

1

2

CONNECTING OBSERVED MICROBURST PRECIPITATION WITH ITS  
SCATTERING MECHANISM

3

by

Mykhaylo Sergeevich Shumko

4

A dissertation submitted in partial fulfillment  
of the requirements for the degree

of

Doctor of Philosophy

in

Physics

5

MONTANA STATE UNIVERSITY  
Bozeman, Montana

October 2019

6

7

©COPYRIGHT

8

by

Mykhaylo Sergeevich Shumko

2019

All Rights Reserved

## DEDICATION

<sup>9</sup> I dedicate this to all MSU students who use L<sup>A</sup>T<sub>E</sub>X. Dedication is optional  
<sup>10</sup> and may be no longer than one page, single spaced, and should precede the  
<sup>11</sup> acknowledgments page.

## ACKNOWLEDGEMENTS

<sup>12</sup> I would like acknowledge the countless engineers, technicians, and scientists who  
<sup>13</sup> made the FIREBIRD, AC-6, and RBSP missions a success. This work was supported  
<sup>14</sup> by Montana State University and by NASA Headquarters under the NASA Earth and  
<sup>15</sup> Space Science Fellowship Program - Grant 80NSSC18K1204. **Add co-author support.**

## TABLE OF CONTENTS

16	1. INTRODUCTION .....	1
17	Charged Particle Motion in Electric and Magnetic Fields .....	2
18	Particle Populations and Their Interractions in the Magnetosphere .....	8
19	Inner Magnetosphere Populations.....	11
20	Plasmasphere.....	13
21	Ring Current .....	15
22	Radiation Belts.....	16
23	Radiation Belt Particle Sources and Sinks .....	20
24	Adiabatic Heating .....	20
25	Wave Resonance Heating .....	21
26	Particle Losses .....	25
27	Microbursts .....	26
28	Scope of Reserach .....	29
29	2. CHAPTER THREE	
30	MICROBURST SCALE SIZE DERIVED FROM MULTIPLE BOUNCES	
31	OF A MICROBURST SIMULTANEOUSLY OBSERVED WITH	
32	THE FIREBIRD-II CUBESATS .....	31
33	Contribution of Authors and Co-Authors .....	31
34	Manuscript Information .....	32
35	Key Points .....	33
36	Abstract .....	33
37	Introduction .....	34
38	Spacecraft and Observation .....	36
39	Analysis .....	39
40	Electron Bounce Period .....	40
41	Microburst Energy Spectra .....	42
42	Microburst Scale Sizes .....	42
43	Discussion and Conclusions .....	45
44	Acknowledgments .....	47
45	3. CONCLUSION .....	48
46	4. REFERENCES CITED.....	49
47	APPENDIX: Appendix A.....	56
48	Time and position correction .....	56

## LIST OF FIGURES

Figure	Page
49      1.1 The three periodic motions of charged particles 50      in Earth's dipole magnetic field. These motions 51      are: gyration about the magnetic field line, bounce 52      motion between the magnetic poles, and azimuthal 53      drift around the Earth. Figure from (Baumjohann 54      and Treumann, 1997). ....	2
55      1.2 Charged particle motion in a uniform magnetic field 56 $\vec{B}$ . Panel (A) shows the geometry defining the 57      pitch angle, $\alpha$ . Panel (B) and (C) show two helical 58      electron trajectories with dashed lines assuming a 59      large and small $\alpha$ (corresponding to a small and large 60      parallel velocity $v_{  }$ ), respectively. ....	6
61      1.3 Contours of constant gyration, bounce, and drift 62      frequencies for electrons and protons in a dipole field. 63      Figure from Schulz and Lanzerotti (1974). ....	7
64      1.4 Macroscopic structures in the outer magnetosphere. 65      The solar wind with its frozen-in interplanetary 66      magnetic field is shown on the left and is traveling 67      supersonically towards the right. The solar wind 68      envelops Earth's magnetic field to create the mag- 69      netosphere cavity. Since the solar wind is traveling 70      supersonically, it creates a bow shock up stream. 71      Downstream of the bow shock the shocked solar wind 72      plasma inside the magnetosheath flows around the 73      magnetopause, a boundary between the solar wind 74      and magnetosphere. Figure from Baumjohann and 75      Treumann (1997). ....	9
76      1.5 Macroscopic structures in the inner magnetosphere 77      most relevant to this dissertation. The plasmas- 78      phere, and the radiation belts are shown and ring 79      current is co-located there as well. Sun is to the left. 80      Figure from Baumjohann and Treumann (1997). ....	10
81      1.6 The series of steps involved in magnetic reconnection 82      with a southward IMF. Figure from Baumjohann 83      and Treumann (1997). ....	12

## LIST OF FIGURES – CONTINUED

Figure	Page
84      1.7 Equipotential lines and electric field arrows due to 85      the superposition of the co-rotation and convection 86      electric fields. Electrons in the shaded region execute 87      closed orbits. Outside of the shaded regions the 88      electrons are not trapped and will escape. The 89      region separating the two regimes is called the Alfvén 90      layer. Figure from Baumjohann and Treumann (1997).....	14
91      1.8 The DST index during the St. Patrick's Day 2015 92      storm. This storm was caused by a coronal mass 93      ejection on March 15th, 2015. The storm phases 94      are: initial phase, main phase, and recovery phase. 95      The initial phase occurred when the Dst peaked at 96      +50 nT on March 17th during which the ring current 97      was eroded by the coronal mass ejection during the 98      interval shown by the red bar. Then the rapid 99      decrease to $\approx -200$ nT was during the main phase 100     where many injections from the magnetotail pumped 101     up the ring current which reduced Earth's magnetic 102     field strength at the ground and is shown with the 103     green bar. Lastly, the recovery phase lasted from 104     March 18th to approximately March 29th during 105     which the ring current particles were lost and the 106     ring current returned to its equilibrium state. The 107     recovery phase is shown with the blue bar.....	17
108     1.9 The two radiation belts with a the locations of 109     various satellites and orbits. Figure from (Horne 110     et al., 2013). .....	18
111     1.10 The dynamics of the outer radiation belt in 1997 112     from the POLAR satellite. Top panel shows the 1.2- 113     2.4 MeV electron flux as a function of L and 1997 day 114     of year. The middle panel shows the DST index, and 115     bottom panel shows the solar wind velocity. Figure 116     from (Reeves et al., 2003). .....	19

## LIST OF FIGURES – CONTINUED

Figure	Page
117      1.11 The trajectories of an electron and a right-hand circularly polarized wave during a cyclotron resonance. The electron's $v_{\parallel}$ and the wave's $k_{\parallel}$ are in opposite directions such that the wave's frequency is Doppler shifted to a integer multiple of the electron cyclotron frequency. Figure from (Tsurutani and Lakhina, 1997). ....	22
123      1.12 Various wave modes in the magnetosphere. Ultra low frequency waves occur through the magnetosphere. Chorus waves are typically observed in the 0-12 midnight-dawn region. EMIC waves are typically observed in the dusk MLT sector. Hiss waves are observed inside the plasmasphere. Figure from Millan and Thorne (2007). ....	24
130      1.13 An example train of microbursts observed by FIREBIRD-II unit 4 on February 2nd, 2015. The colored curves show the differential energy channel count rates in six channels from $\approx 200$ keV to greater than 1 MeV. The x-axis labels show auxiliary information such as time of observation and the spacecraft position in L, MLT, latitude and longitude coordinates. ....	27
137      1.14 Relativistic ( $> 1$ MeV) distribution of microburst occurrence rates as a function of L and MLT. The three panels show the microburst occurrence rate dependence on geomagnetic activity, parameterized by the auroral electrojet (AE) index for (a) $AE < 100$ nT, (b) $100 < AE < 300$ nT and (c) $AE > 300$ nT. Figure from Douma et al. (2017)....	28

## LIST OF FIGURES – CONTINUED

Figure	Page
144      2.1 HiRes data of the microburst observed at February 145      2nd, 2015 at 06:12:53 UT, smoothed with a 150 ms 146      rolling average. The subsequent bounces showed 147      some energy dispersion. As discussed in Appendix 148      A, a time correction of -2.28 s was applied to FU3. 149      While the flux from five energy channels is shown, 150      only channels with reasonable counting statistics 151      were used for the spatial scale analysis. Vertical 152      colored bars show the $\sqrt{N}$ error every 10th data 153      point and vertical black bars are lined up with the 154      peaks in the 220-283 keV energy channel to help 155      identify dispersion. ....	38
156      2.2 Observed and theoretical $t_b$ for electrons of energies 157      from 200 to 770 keV. The solid black line is $t_b$ 158      in a dipole magnetic field, derived in Schulz and 159      Lanzerotti (1974). The red dotted and cyan dashed 160      lines are the $t_b$ derived using the T89, and T04 161      magnetic field models with IRBEM-Lib. Lastly, 162      the blue dot-dash curve is the $t_b$ derived using the 163      Olson & Pfitzer Quiet model. The green and purple 164      rectangles represent the observed $t_b$ for FU3 and 165      FU4 using a Gaussian fit, respectively. The blue 166      rectangles represent the observed $t_b$ calculated with 167      the minima between the bounces. The width of the 168      boxes represent the width of those energy channels, 169      and the height represents the uncertainty from the fit.....	41

## LIST OF FIGURES – CONTINUED

Figure	Page
170      2.3 The topology of the FIREBIRD-II orbit and the 171      multiple bounces of the microburst projected onto 172      latitude and longitude with axis scaled to equal 173      distance. Attributes relating to FU3 shown in red 174      dashed lines, and FU4 with blue solid lines. The 175      spacecraft path is shown with the diagonal lines, 176      starting at the upper right corner. The labels P1- 177      4 for FU4 and P1-5 for FU3 indicate where the 178      spacecraft were when the $N^{th}$ peak was seen in 179      the lowest energy channel in the HiRes data. The 180      stars with the accompanying energy labels represent 181      the locations of the electrons with that energy that 182      started at time of P1, and were seen at the last peak 183      on each spacecraft. The rectangles represent the 184      lower bound of the microburst scale size, assuming 185      that the majority of the electrons were in the upper 186      boundary of energy channel 4.....	44
187      A.1 Cross-correlation time lag analysis applied to a train 188      of microbursts. Panel (a) and (b) show the count 189      rate from the lowest energy channel. Panel (c) shows 190      the cross-correlation coefficient as a function of time 191      lag. Panel (d) shows the shifted timeseries. Clock 192      difference was 2.23 s.....	58
193      A.2 Same analysis as Fig. A.1 on a different time period. 194      Clock difference was 2.21 s.....	59
195      A.3 Same analysis as Fig. A.1 on a different time period. 196      Clock difference was 2.25 s.....	60
197      A.4 Same analysis as Fig. A.1 on a different time period. 198      Clock difference was 2.27 s.....	61
199      A.5 Same cross-correlation time lag analysis applied to 200      stationary spatial structures. The cross-correlation 201      lag between these events is a sum of the clock differ- 202      ence and time lag due to the spacecraft separation. 203      The lag derived at this time was 4.95 s.....	62

## LIST OF FIGURES – CONTINUED

	Figure	Page
204	A.6 Same analysis as Fig. A.5 applied to a different	
205	stationary spatial feature. The lag derived at this	
206	time was 5.01 s. ....	63

## NOMENCLATURE

207

- $\mu$  Dynamic viscosity
- $\mathbf{n}$  Normal vector
- $\mathbf{u}$  Velocity vector

## INTRODUCTION

209        Above Earth's atmosphere are the a pair of Van Allen radiation belts, a complex  
210      and dynamic plasma environment that effects our technology-driven society. These  
211      effects include: a higher radiation dose for astronauts and cosmonauts, higher chance  
212      of spacecraft failure due to single event upsets that can lead to catastrophic latchups,  
213      degradation of silicon (changing the silicon doping) from an extended radiation dose  
214      that can degrade a transistor to the point where it no longer function as a switch,  
215      and the degradation of the ozone layer due to the chemical production of  $\text{NO}_X$  and  
216       $\text{HO}_X$  molecules. With these effects in mind, it is no surprise that the radiation belts  
217      have been extensively studied since their discovery in the 1960s.

218        One natural phenomenon in the radiation belts that has been a topic of interest  
219      in the space physics community is wave-particle intersections that, as we will explore  
220      throughout this dissertation, can accelerate particles to very high energies (e.g.  $\approx$   
221      MeV for electrons) and scatter them into the atmosphere.

222        The goal of this dissertation is to study the wave-particle mechanism that  
223      scatters microbursts, a sub-second impulse of electrons into Earth's atmosphere.  
224        Before we dive deep into the physics of wave-particle interactions, an introduction to  
225      Earth's magnetosphere is warranted. Single charged particle motion in Earth's electric  
226      and magnetic fields will be described first. Then the major particle populations in  
227      the magnetosphere and the coupling between them will be described. Lastly, a brief  
228      overview of wave-particle interactions and their effects will be presented.

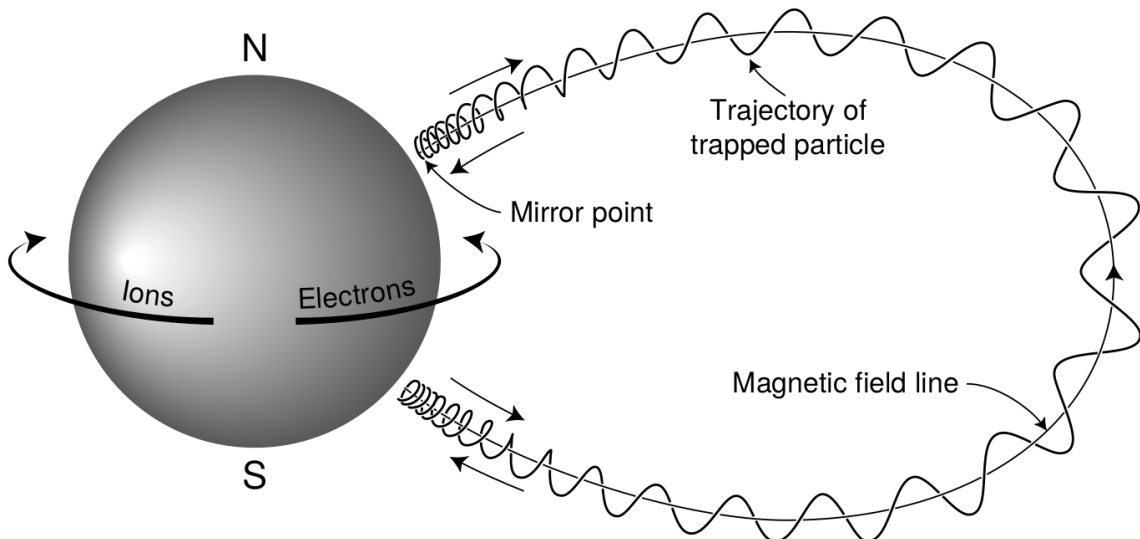


Figure 1.1: The three periodic motions of charged particles in Earth's dipole magnetic field. These motions are: gyration about the magnetic field line, bounce motion between the magnetic poles, and azimuthal drift around the Earth. Figure from (Baumjohann and Treumann, 1997).

<sup>229</sup>

### Charged Particle Motion in Electric and Magnetic Fields

A charged particle trapped in the magnetosphere will experience three types of periodic motion in Earth's nearly dipolar magnetic field. The three motions are ultimately due to the Lorentz force that a particle of momentum  $\vec{p}$ , charge  $q$ , and velocity  $\vec{v}$  experiences in an electric field  $\vec{E}$  and magnetic field  $\vec{B}$  and is given by

$$\frac{d\vec{p}}{dt} = q(\vec{E} + \vec{v} \times \vec{B}). \quad (1.1)$$

- <sup>230</sup> In the magnetosphere, the three periodic motions in decreasing frequency are gyration,  
<sup>231</sup> bounce, and drift and are schematically shown in Fig. 1.1. Each of these  
<sup>232</sup> motions have a corresponding conserved quantity i.e. an adiabatic invariant.

The highest frequency periodic motion is gyration about a magnetic field of

magnitude  $B$ . This motion is circular with a Larmor radius of

$$r = \frac{mv_{\perp}}{|q|B} \quad (1.2)$$

where  $m$  is the mass and  $v_{\perp}$  the particle's velocity perpendicular to  $\vec{B}$ . This motion has a corresponding gyrofrequency

$$\Omega = \frac{|q|B}{m} \quad (1.3)$$

in units of radians/second. Inside the radiation belts the electron gyrofrequency,  $\Omega_e$  is on the order of a kHz. The corresponding adiabatic invariant is found by integrating the particle's canonical momentum around the particle's path of gyration

$$J_i = \oint (\vec{p} + q\vec{A}) \cdot d\vec{l} \quad (1.4)$$

where  $J_i$  is the  $i^{th}$  adiabatic invariant and  $\vec{A}$  is the magnetic vector potential. This integral is carried out by integrating the first term over the circumference of the gyro orbit and integrating the second term using Stokes theorem to calculate the magnetic flux enclosed by the gyro orbit. With suitable integration,  $J_1 \sim v_{\perp}^2/B$  and is conserved as the frequency of the driving force,  $\omega$  satisfies  $\omega \ll \Omega_e$ .

The second highest frequency periodic motion is bouncing due to a parallel gradient in  $\vec{B}$ . This periodic motion naturally arises in the magnetosphere because Earth's magnetic field is stronger near the poles, and artificially in the laboratory in magnetic bottle machines. To understand this motion we first we need to define the concept of pitch angle  $\alpha$  as the angle between  $\vec{B}$  and  $\vec{v}$  which is schematically shown in Fig. 1.2a. The pitch angle relates  $v$  with  $v_{\perp}$ , and  $v_{||}$  (the component of the particles velocity parallel to  $\vec{B}$ ). As shown in 1.2b and c, a larger  $\alpha$  will tighten the

<sup>245</sup> particle's helical trajectory and vice versa.

Assuming the particle's kinetic energy is concerned, the conservation of  $J_1$  implies that given a particle's  $v_{\perp}(0)$  and  $B(0)$  at the magnetic equator (where Earth's magnetic field is usually at a minimum), we can calculate its  $v_{\perp}(s)$  along the particle's path  $s$  by calculating  $B(s)$  from magnetic field models. The particle's perpendicular velocity is then related via

$$\frac{v_{\perp}^2(0)}{B(0)} = \frac{v_{\perp}^2(s)}{B(s)} \quad (1.5)$$

<sup>246</sup> which can be rewritten as

$$\frac{v^2 \sin^2 \alpha(0)}{B(0)} = \frac{v^2 - v_{\parallel}^2(s)}{B(s)} \quad (1.6)$$

<sup>247</sup> and re-arranged to solve for  $v_{\parallel}(s)$

$$v_{\parallel}(s) = v \sqrt{1 - \frac{B(s)}{B(0)} \sin^2 \alpha(0)} \quad (1.7)$$

<sup>248</sup> which will tend towards 0 when the second term in the radical approaches 1.

<sup>249</sup> The location where  $v_{\parallel}(s) = 0$  is called the mirror point and is where a particle  
<sup>250</sup> stops and reverses direction. Since Earth's magnetic field is stronger towards the  
<sup>251</sup> poles, the mirroring particle will execute periodic bounce motion between its two  
<sup>252</sup> mirror points in the northern and southern hemispheres. The corresponding adiabatic  
<sup>253</sup> invariant,  $J_2$  is

$$J_2 = \oint p_{\parallel} ds \quad (1.8)$$

where  $ds$  describes the particle path between the mirror points in the northern and southern hemispheres (see Fig. 1.1).  $J_2$  is found by substituting Eq. 1.7 into Eq. 1.8 and defining the magnetic field strength at the mirror points as  $B_m$  where  $\alpha(m) = 90^\circ$ .

The  $J_2$  integral can be written as

$$J_2 = 2p \int_{m_n}^{m_s} \sqrt{1 - \frac{B(s)}{B(m)}} ds \quad (1.9)$$

where  $m_n$  and  $m_s$  are the northern and southern mirror points, respectively. The bounce period can be estimated (e.g. Baumjohann and Treumann, 1997) to be

$$t_b \approx \frac{LR_e}{\sqrt{W/m}} (3.7 - 1.6 \sin \alpha(0)) \quad (1.10)$$

where  $L$  is the  $L$ -shell which describes the distance from the Earth's center to the location where a particular magnetic field line crosses the magnetic equator, in units of Earth radii,  $R_e$ .  $W$  is the particle's kinetic energy. As with gyration, a particle bounces as long as  $\omega \ll \Omega_b$ , where  $\Omega_b$  is the bounce frequency.

At this stage it is instructional to introduce the notion of the loss cone pitch angle,  $\alpha_L$ . A particle with  $\alpha \leq \alpha_L$  will mirror at or below  $\approx 100$  km altitude in the atmosphere. A particle at those altitudes will encounter Earth's atmosphere and has a significant probability of Coulomb scattering with atmospheric particles and be lost to the atmosphere.

The slowest periodic motion experienced by charged particles in Earth's magnetic field is azimuthal drift around the Earth. This drift results from a combination of a radial gradient in  $\vec{B}$  and the curvature of the magnetic field. The radial gradient drift arises because Earth's magnetic field is stronger near the Earth where the particle's gyroradius radius of curvature is smaller as it gyrates towards stronger magnetic field, and larger when it gyrates outward. The overall effect is the particle gyro orbit does not close on itself and negatively charged particles drift East and positively charged particles drift West. The radial gradient drift is enhanced by the centrifugal force that a particle experiences as it bounces along the curved field lines. The drift adiabatic

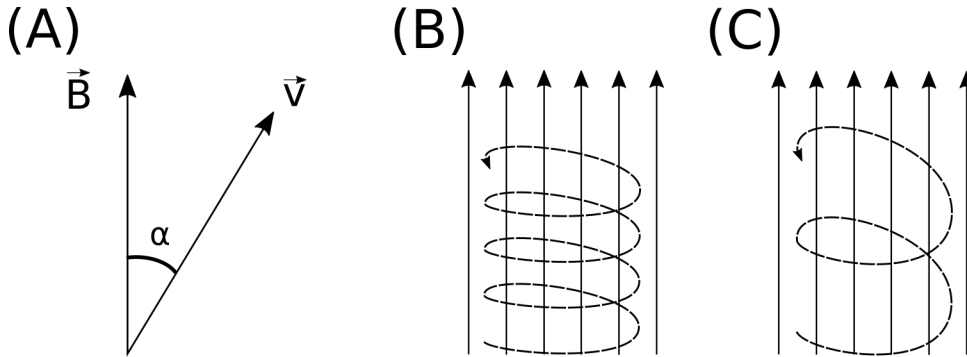


Figure 1.2: Charged particle motion in a uniform magnetic field  $\vec{B}$ . Panel (A) shows the geometry defining the pitch angle,  $\alpha$ . Panel (B) and (C) show two helical electron trajectories with dashed lines assuming a large and small  $\alpha$  (corresponding to a small and large parallel velocity  $v_{||}$ ), respectively.

<sup>274</sup> invariant,  $J_3$  is found by integrating Eq. 1.4 over the complete particle orbit around  
<sup>275</sup> the Earth. The shape of this drift orbit is otherwise known as a drift shell. For  $J_3$ ,  
<sup>276</sup> the first term is negligible and the second term is the magnetic flux enclosed by the  
<sup>277</sup> drift shell,  $\Phi_m$  i.e.  $J_3 \sim \Phi_m$ .

<sup>278</sup> Figure 1.3 from Schulz and Lanzerotti (1974) shows contours of the gyration,  
<sup>279</sup> bounce, and drift frequencies for electrons and protons in Earth's dipole magnetic  
<sup>280</sup> field.

Up until now we have considered the three periodic motions due Earth's magnetic field and the absence of electric fields. If  $\vec{E}$  is present, a particle's center of gyration i.e., averaged position of the particle over a gyration, will drift with a velocity perpendicular to both  $\vec{E}$  and  $\vec{B}$ . The drift velocity can be solved directly from Eq. 1.1 and is

$$\vec{v}_E = \frac{\vec{E} \times \vec{B}}{B^2}. \quad (1.11)$$

<sup>281</sup> Lastly, for more detailed derivations of these motions, see the following texts:  
<sup>282</sup> Baumjohann and Treumann (1997); Schulz and Lanzerotti (1974); Tsurutani and  
<sup>283</sup> Lakhina (1997).

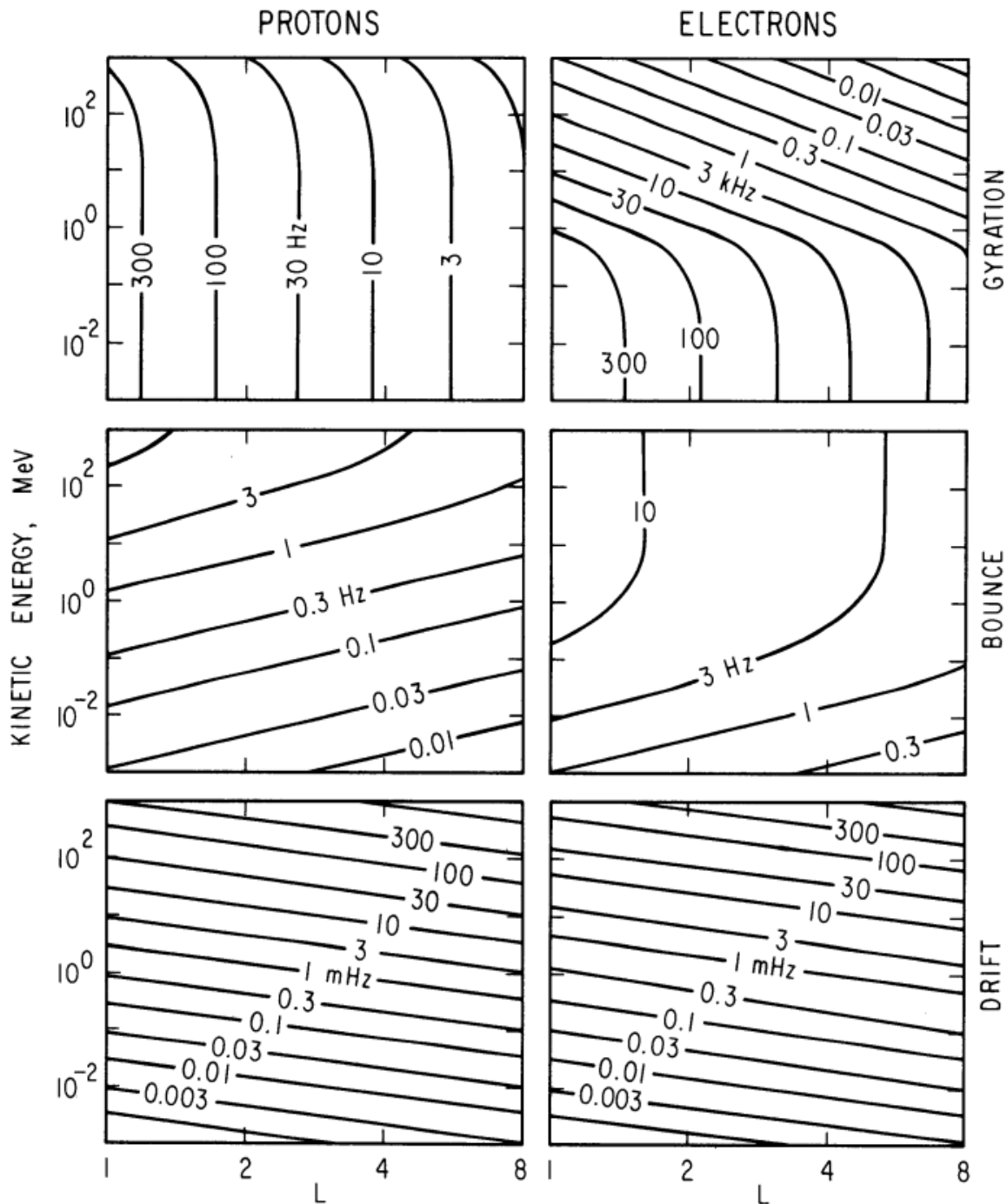


Figure 1.3: Contours of constant gyration, bounce, and drift frequencies for electrons and protons in a dipole field. Figure from Schulz and Lanzerotti (1974).

284        Particle Populations and Their Interractions in the Magnetosphere

285        The single-particle motion in Earth's magnetic field described in the previous  
286        section is a prerequisite to understanding how magnetospheric particles organize into  
287        macroscopic populations. The structure of the outer magnetosphere is shown in Fig.  
288        1.4 and inner magnetosphere in Fig. 1.5. In this section we will introduce the various  
289        particle populations in the magnetosphere and how they couple.

290        The sun and its solar wind are ultimately the source of energy input into the  
291        magnetosphere. The solar wind at Earth's orbit is a plasma traveling at supersonic  
292        speeds with an embedded interplanetary magnetic field (IMF). When the solar wind  
293        encounters Earth's magnetic field the plasma can not easily penetrate into the  
294        magnetosphere, rather it drapes around the magnetosphere forming a cavity in the  
295        solar wind that is roughly shaped as shown in Fig. 1.4. Because the solar wind is  
296        supersonic at 1 AU, a bow shock exists upstream of the magnetosphere. The solar  
297        wind plasma, after it is shocked by the bow shock, flows around the magnetosphere  
298        inside the magnetosheath. The surface where the solar wind ram pressure and Earth's  
299        magnetic pressure balance is termed the magnetopause, which can be thought of as  
300        a boundary between the solar wind's and Earth's plasma environments. This is  
301        a slightly naive description of the magnetopause, but is nonetheless an instructive  
302        conceptual picture. The shocked plasma then flows past the Earth where it shapes  
303        the magnetotail. In the magnetotail the solar wind magnetic pressure balances Earth's  
304        magnetic field pressure in the lobes. The magnetotail extends on the order of 100  
305         $R_E$  downstream of Earth [Add citation](#), and the tailward stretching of magnetic field  
306        lines creates the plasma sheet which exists in the region of low magnetic field strength  
307        near the magnetic equator [Add citation](#). The plasma sheet flows from dusk to dawn  
308        (out of the page in Figs. 1.4 and 1.5) and this current is connected to a zoo of other

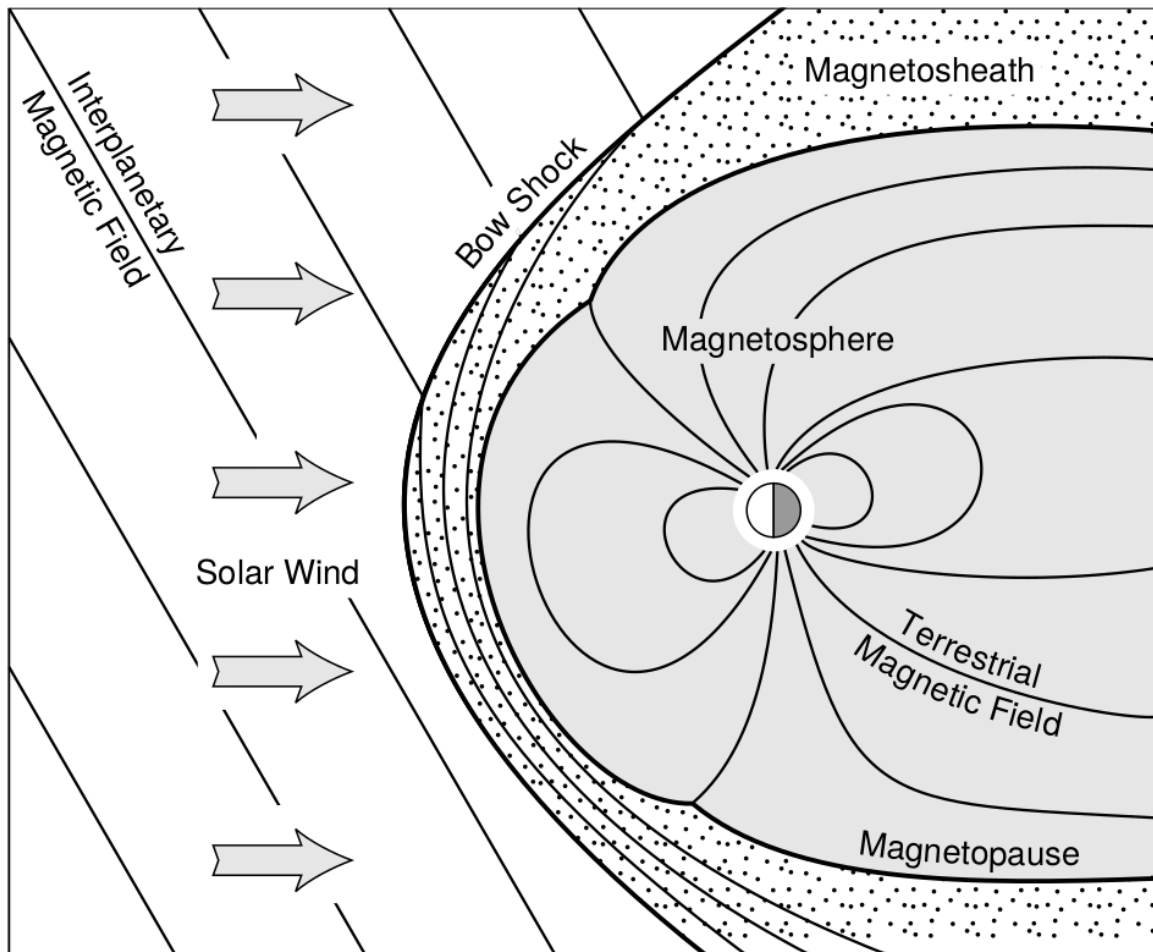


Figure 1.4: Macroscopic structures in the outer magnetosphere. The solar wind with its frozen-in interplanetary magnetic field is shown on the left and is traveling supersonically towards the right. The solar wind envelops Earth's magnetic field to create the magnetosphere cavity. Since the solar wind is traveling supersonically, it creates a bow shock up stream. Downstream of the bow shock the shocked solar wind plasma inside the magnetosheath flows around the magnetopause, a boundary between the solar wind and magnetosphere. Figure from Baumjohann and Treumann (1997).

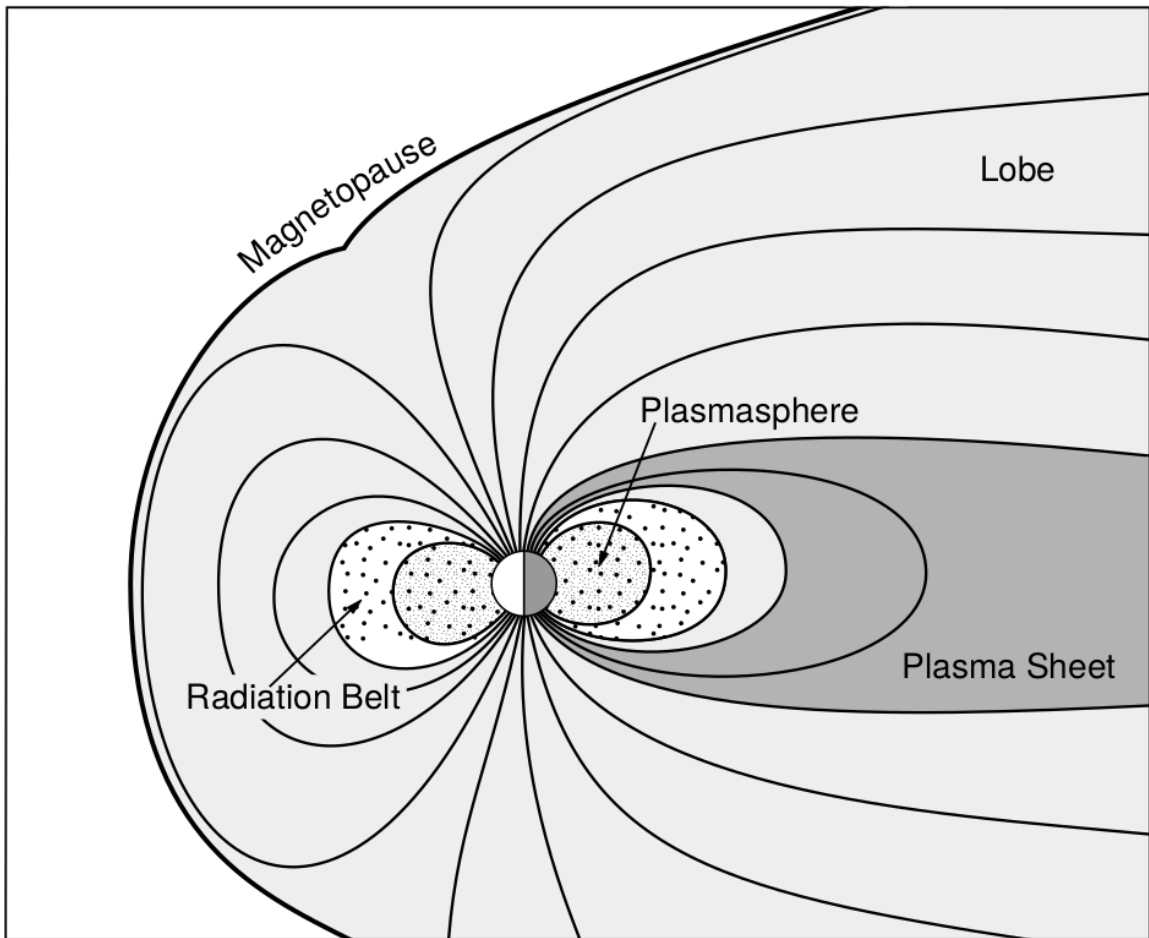


Figure 1.5: Macroscopic structures in the inner magnetosphere most relevant to this dissertation. The plasmasphere, and the radiation belts are shown and ring current is co-located there as well. Sun is to the left. Figure from Baumjohann and Treumann (1997).

309 currents in the magnetosphere which is beyond the scope of this dissertation.

310 The idea of the magnetopause as a barrier between the solar wind and  
 311 the magnetosphere is not entirely accurate due to the presence of reconnection.  
 312 Reconnection was first conceived by Dungey (1961) who described the convection of  
 313 Earth's magnetic field between the bow and tail regions of the magnetosphere. This  
 314 process is known as the Dungey cycle and is most effective when the IMF is pointing  
 315 southward as is shown in Fig. 1.6 part 1. As the IMF contacts Earth's magnetic  
 316 field it reconnects with it so that Earth's magnetic field is directly connected to the  
 317 IMF. Then as the solar wind flows tailward the IMF drags Earth's magnetic field  
 318 towards the magnetotail as shown in Fig. 1.6 parts 2-6. As more and more magnetic  
 319 field lines are draped in the magnetotail, magnetic pressure increases in the lobes  
 320 which squeezes the plasma sheet until Earth's magnetic field reconnects as is shown  
 321 in Fig. 1.6 part 7. Lastly, Fig. 1.6 part 8 shows the newly merged magnetic field  
 322 line and the plasma frozen on it moves Earthward under the magnetic tension force  
 323 to become more dipolar. This is called a dipolarization of the magnetic field, and the  
 324 plasma frozen on these field lines can be observed as injections (e.g. Turner et al.,  
 325 2015). Injection of plasma into the inner magnetosphere is one of the drivers of inner  
 326 magnetosphere dynamics. Should I talk about the K-H instability and how there  
 327 could be micro reconnection? i.e. cite a paper or two that support or refute that  
 328 idea.

329 Inner Magnetosphere Populations

330 Before we describe the inner magnetosphere particle populations, we first need to  
 331 describe the coordinate system used to organize the inner magnetosphere populations.  
 332 The first coordinate was defined in section 1 and is the L shell. L shell can be thought  
 333 of as an analogue to a radius but in a dipole geometry. The azimuthal coordinate

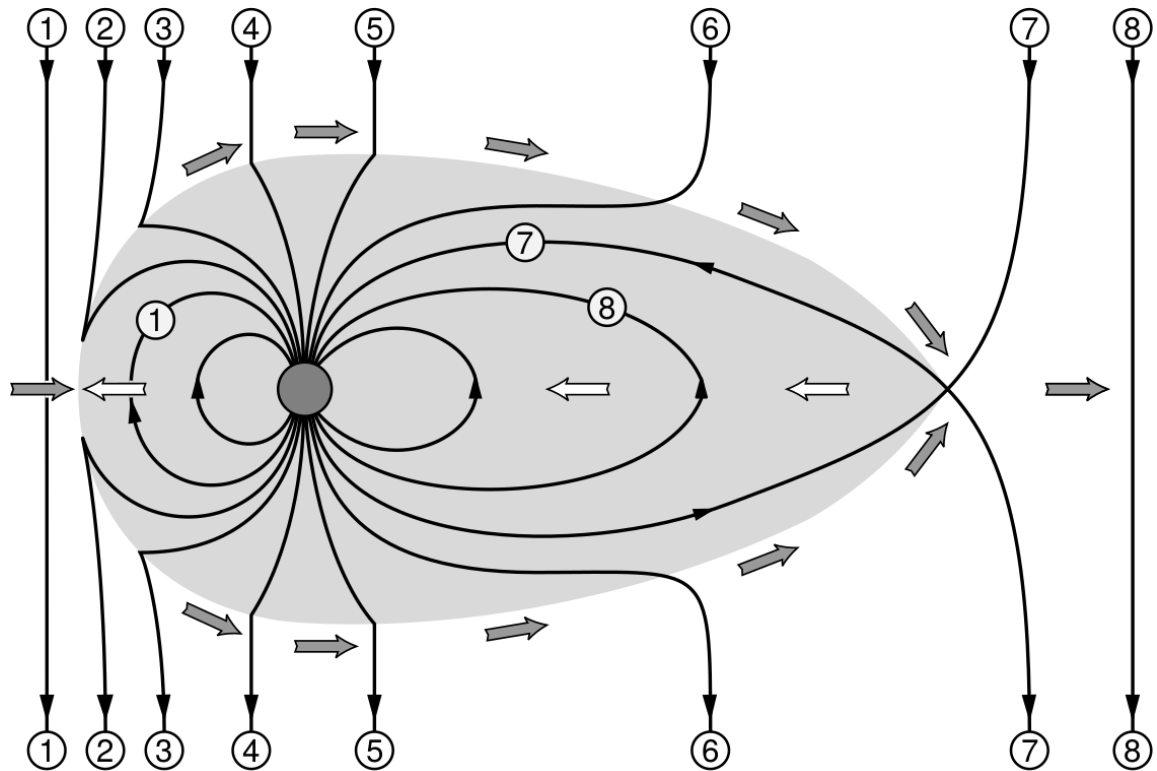


Figure 1.6: The series of steps involved in magnetic reconnection with a southward IMF. Figure from Baumjohann and Treumann (1997).

334 is the magnetic local time (MLT). For an observer above Earth's north pole looking  
 335 down, MLT is defined to be 0 (midnight) in the anti-sunward direction, and increases  
 336 in the counter-clockwise direction with 6 at dawn, 12 at noon (sunward direction),  
 337 and 18 in dusk. The last coordinate used in this dissertation is the magnetic latitude,  
 338  $\lambda$  which is analogous to the latitude coordinate and is defined to be 0 at the magnetic  
 339 equator.

340 The low energy particle dynamics in the inner magnetosphere are organized by  
 341 two electric fields: the co-rotation and the dawn-dusk electric fields. The co-rotation  
 342 electric field arises from the rotation of Earth's magnetic field. Since particles are  
 343 frozen on magnetic field lines and the plasma conductivity is effectively infinite, to  
 344 a non-rotating observer, Earth's rotation appears as a radial electric field that drops  
 345 off as  $\sim L^2$ . This electric field makes particles orbit around the Earth due to the  
 346  $\vec{E} \times \vec{B}$  drift. The other electric field, pointing from dawn to dusk is called the  
 347 convection electric field and is formed by the Earthward transport of particles from  
 348 the magnetotail that appears as an electric field to a stationary observer (with respect  
 349 to Earth). The superposition of the co-rotation and convection electric fields  
 350 results in a potential field shown in Fig. 1.7. The shaded area in Fig. 1.7 shows  
 351 the orbits on which low energy electrons are trapped, and outside are the untrapped  
 352 particles. The dynamic topology of the shaded region in Fig. 1.7 is controlled by only  
 353 the convection electric field which is dependent on the solar wind speed and the IMF.  
 354 The lowest energy particles, that are most effected by these electric fields, make up  
 355 the plasmasphere.

356 Plasmasphere The plasmasphere is a dense ( $n_e \sim 10^3/\text{cm}^3$ ), cool plasma  
 357 ( $\sim \text{eV}$ ) that extends to  $L \sim 4$  (extent is highly dependent on the solar wind and  
 358 magnetospheric conditions) and is sourced from the ionosphere. The two main

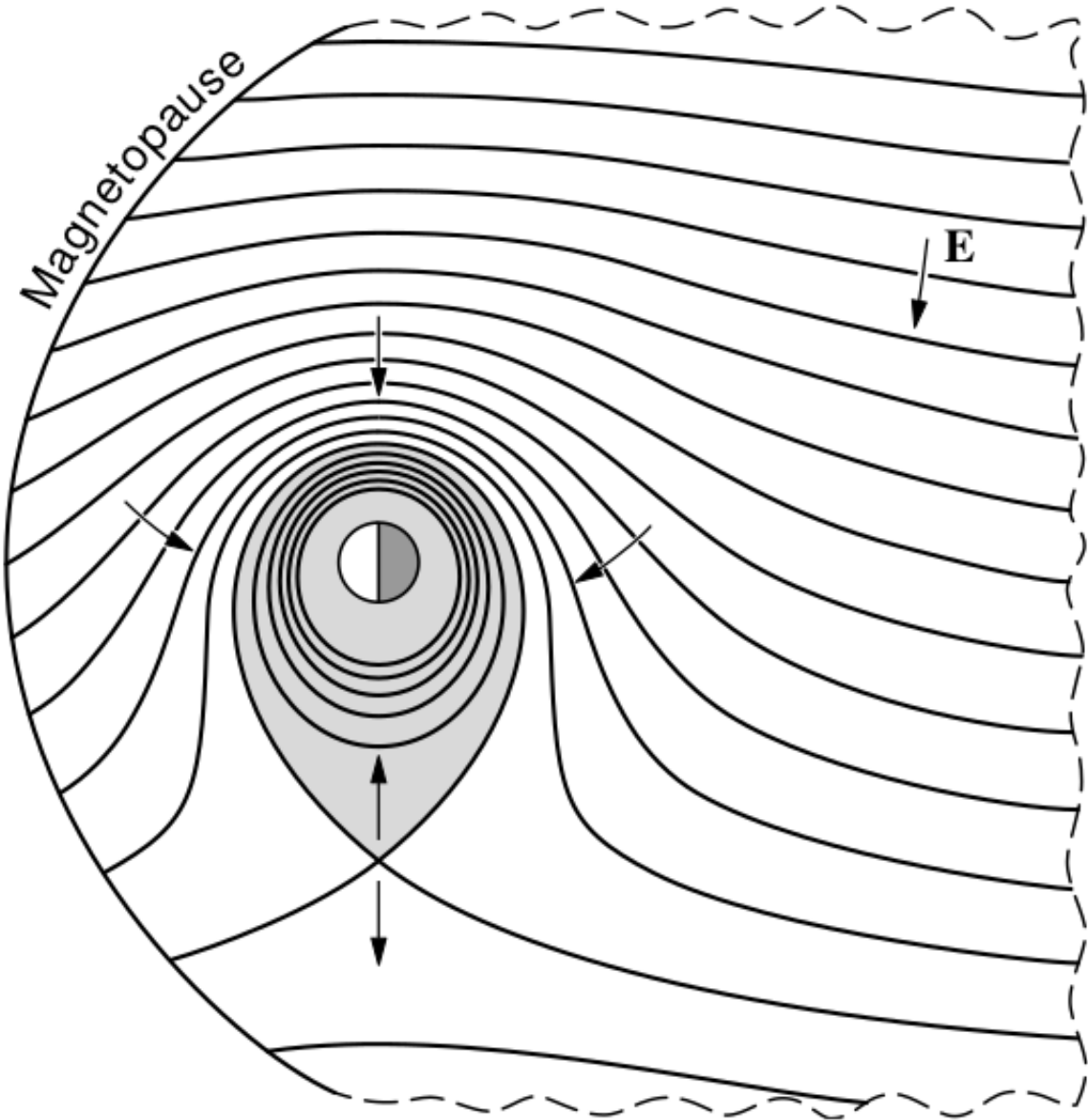


Figure 1.7: Equipotential lines and electric field arrows due to the superposition of the co-rotation and convection electric fields. Electrons in the shaded region execute closed orbits. Outside of the shaded regions the electrons are not trapped and will escape. The region separating the two regimes is called the Alfvén layer. Figure from Baumjohann and Treumann (1997).

359 mechanisms that source the cold plasma from the ionosphere are ultraviolet ionization  
 360 by sunlight and particle precipitation. The ultraviolet ionization by sunlight is  
 361 strongly dependent on the time of day (day vs night), latitude (more ionization near  
 362 the equator). The ionization due to particle precipitation, on the other hand, is highly  
 363 dependent on magnetospheric conditions, and mostly occurs at high latitudes.

364 The outer boundary of the plasmasphere is the plasmapause which is typically  
 365 identified as a steep radial gradient in plasma density from  $\sim 10^3/\text{cm}^3$  to  $\sim 1/\text{cm}^3$ . As  
 366 we will see throughout this dissertation, the location of the plasmapause is important  
 367 to model (e.g. O'Brien and Moldwin, 2003) and understand since the plasma density  
 368 strongly controls the efficiency of particle scattering (Horne et al., 2005).

369 Ring Current The next higher energy population is the ring current. This  
 370 population consists of protons and electrons between tens and a few hundred keV  
 371 that drift around the Earth. The orbits of higher energy particles are not as effected  
 372 by the convection and co-rotation electric field, rather they drift around the Earth  
 373 due to gradient and curvature drifts. Since the direction of the drift is dependent on  
 374 charge, protons drift west around the Earth and electrons drift East. This has the  
 375 effect of creating a current around the Earth.

376 The ring current generates a magnetic field which decreases the magnetic field  
 377 strength on Earth's surface and increases it outside of the ring current. The decrease  
 378 of Earth's magnetic field strength is readily observed by a system of ground-based  
 379 magnetometers and is merged into a Disturbance Storm Time (DST) index. An  
 380 example of a DST index time series from a coronal mass ejection (CME) driven 2015  
 381 St. Patrick's Day storm is shown in Fig. 1.8. The ring current is sometimes first  
 382 depleted and DST increases slightly (initial phase or sudden storm commencement).  
 383 Then the ring current is rapidly built up during which DST rapidly decreases (main

384 phase). Lastly the ring current gradually decays toward its equilibrium state over a  
 385 period of a few days and DST increases towards 0 (recovery phase). The DST index  
 386 along with other indicies are readily used by the space physics community to quantify  
 387 the global state of the magnetosphere.

388        Radiation Belts The highest energy particle populations are in the Van Allen  
 389 radiation belts. These belts were discovered by Van Allen (1959) and Vernov and  
 390 Chudakov (1960) during the Cold War and are a pair of toroidally shaped populations  
 391 of trapped electrons and protons usually within to  $L < 8$  and are shown in Fig. 1.9.  
 392 Their quiescent toroidal shape is similar to the shape of the plasmasphere and ring  
 393 current and is a result of Earth's dipole magnetic field and the conservation of the  
 394 three adiabatic invariants discussed in section 1.

395        The inner radiation belt is extremely stable on time periods of years, extends  
 396 to  $L \approx 2$ , and mainly consists of protons with energies between MeV and GeV and  
 397 electrons with energies up to  $\approx 1$  MeV (Claudepierre et al., 2019). The source of  
 398 inner radiation belt protons is believed to be due to cosmic-ray albedo neutron decay  
 399 (e.g. Li et al., 2017) and inward radial diffusion for electrons (e.g. O'Brien et al.,  
 400 2016). The gap between the inner and outer radiation belt is called the slot, which is  
 401 believed to be due to hiss waves inside the plasmasphere (described below) scattering  
 402 particles into the atmosphere (e.g. Breneman et al., 2015; Lyons and Thorne, 1973).

403        The outer radiation belt, on the other hand is much more dynamic and consists  
 404 of mainly electrons of energies up to a few MeV. The outer belt's spatial extent is  
 405 highly variable e.g. see Fig. 1.10, and is typically observed at  $4 < L < 8$ . Since  
 406 the outer radiation belt contains a dynamic population of energetic particles that  
 407 pose a threat to human and technological presence in Earth's atmosphere and space,  
 408 decades of research has been undertaken to understand and predict the outer radiation

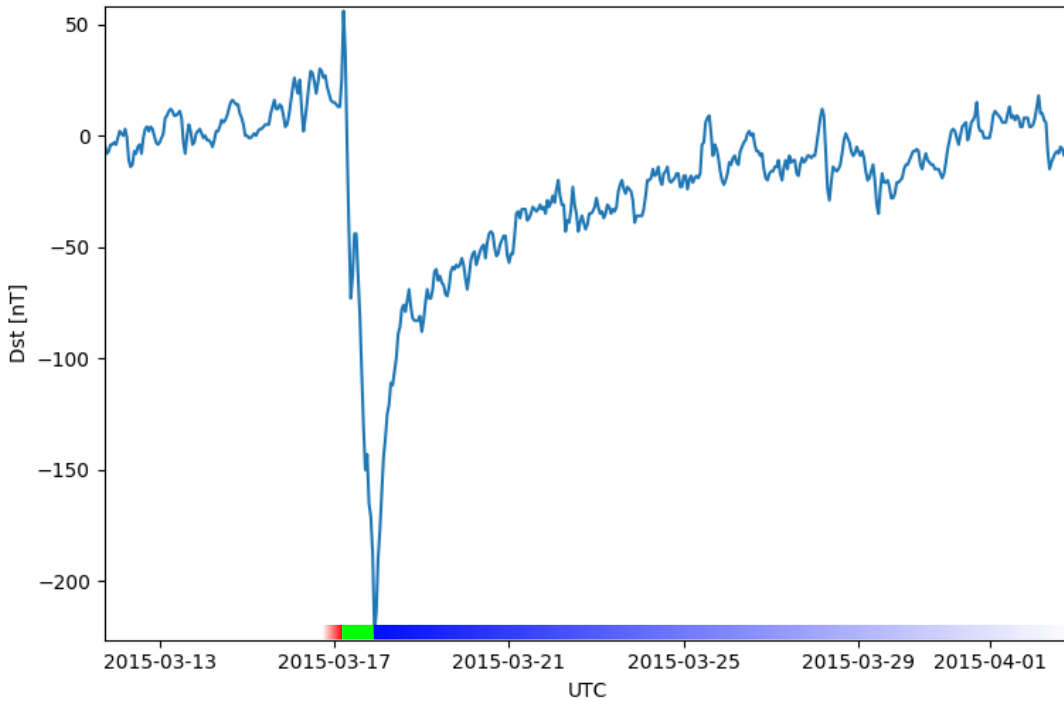


Figure 1.8: The DST index during the St. Patrick's Day 2015 storm. This storm was caused by a coronal mass ejection on March 15th, 2015. The storm phases are: initial phase, main phase, and recovery phase. The initial phase occurred when the Dst peaked at +50 nT on March 17th during which the ring current was eroded by the coronal mass ejection during the interval shown by the red bar. Then the rapid decrease to  $\approx -200$  nT was during the main phase where many injections from the magnetotail pumped up the ring current which reduced Earth's magnetic field strength at the ground and is shown with the green bar. Lastly, the recovery phase lasted from March 18th to approximately March 29th during which the ring current particles were lost and the ring current returned to its equilibrium state. The recovery phase is shown with the blue bar.

## The Earth's Electron Radiation Belts

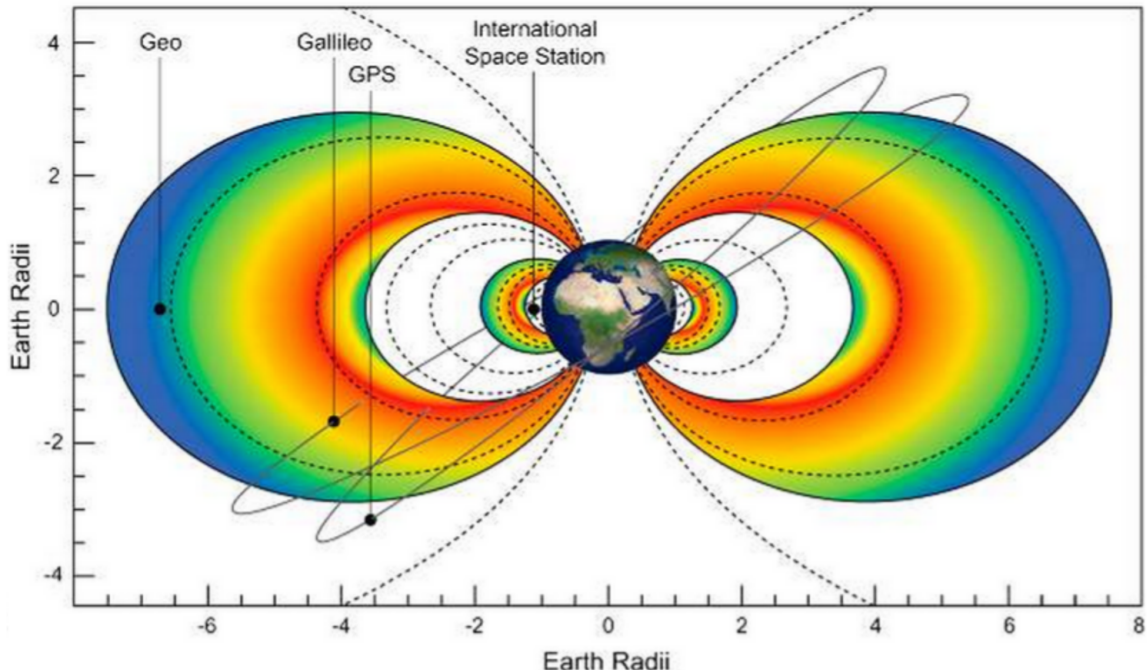


Figure 1.9: The two radiation belts with the locations of various satellites and orbits.  
Figure from (Horne et al., 2013).

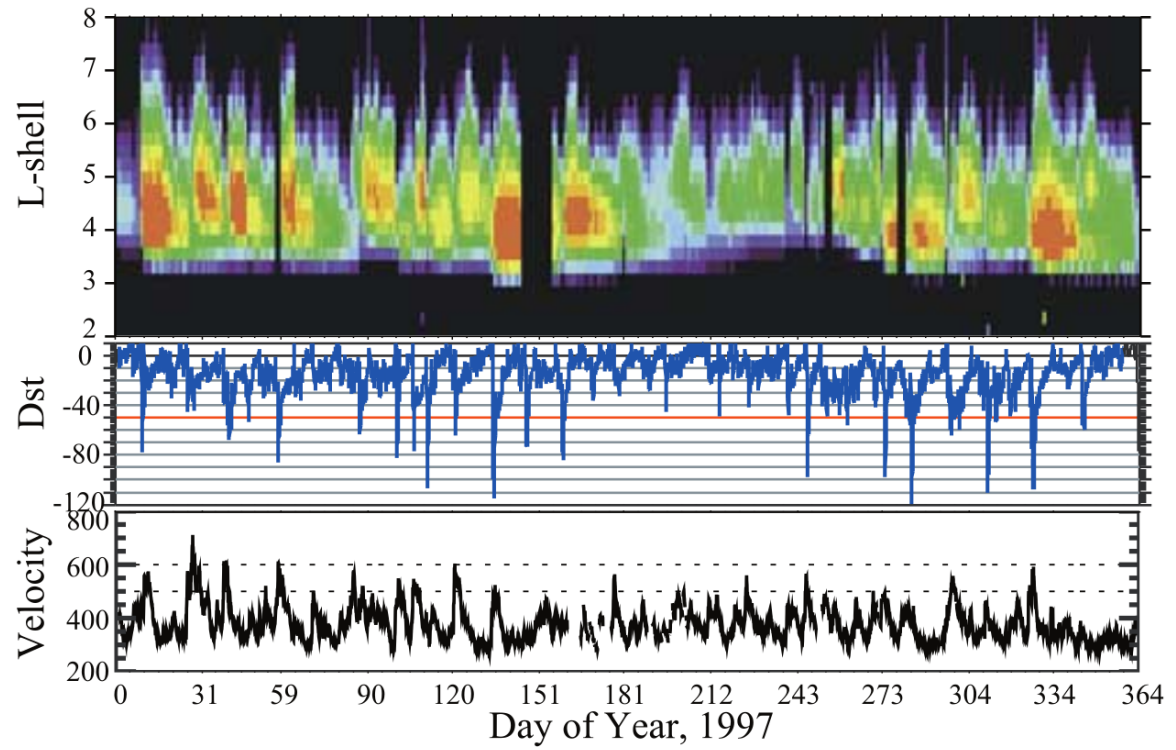


Figure 1.10: The dynamics of the outer radiation belt in 1997 from the POLAR satellite. Top panel shows the 1.2-2.4 MeV electron flux as a function of L and 1997 day of year. The middle panel shows the DST index, and bottom panel shows the solar wind velocity. Figure from (Reeves et al., 2003).

409 belt particles, waves, and wave-particle interactions. The dynamics of the outer  
 410 radiation belt can be understood by considering various competing acceleration and  
 411 loss mechanisms which will be described in the following sections.

412 Radiation Belt Particle Sources and Sinks

413 Adiabatic Heating

414 One of the particle heating and transport mechanisms arises from the Earthward  
 415 convection of particles. The conservation of  $J_1$  implies that the initial and final  $v_\perp$   
 416 depends on the change in the magnetic field amplitude

$$\frac{v_{\perp i}^2}{B_i} = \frac{v_{\perp f}^2}{B_f}. \quad (1.12)$$

417 As a particle convects Earthward,  $B_f > B_i$  thus  $v_\perp$  must increase. The dipole  
 418 magnetic field amplitude can be written as

$$B(L, \theta) = \frac{31.2 \mu\text{T}}{L^3} \sqrt{1 + 3 \cos^2 \theta} \quad (1.13)$$

419 which implies that

$$\frac{v_{\perp f}^2}{v_{\perp i}^2} = \left( \frac{L_i}{L_f} \right)^3. \quad (1.14)$$

420 .

421 In addition, as the particle convects Earthward the distance between the  
 422 particle's mirror points decrease. If  $J_2$  is conserved, the shrinking bounce path implies  
 423 that  $v_{||}$  must increase by

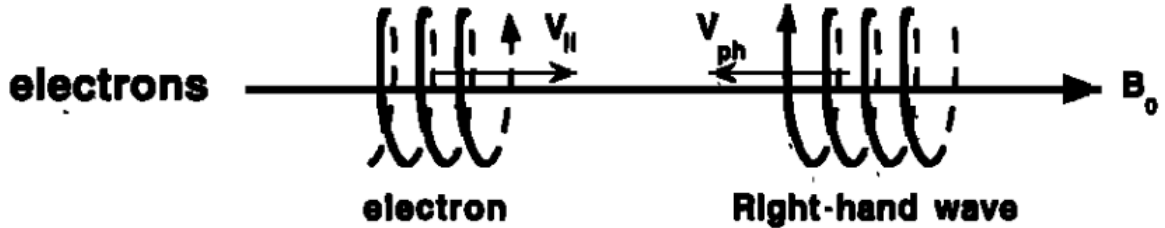
$$\frac{v_{|| f}^2}{v_{|| i}^2} = \left( \frac{L_i}{L_f} \right)^k \quad (1.15)$$

424 where  $k$  ranges from 2 for equatorial pitch angles,  $\alpha_{eq} = 0^\circ$ , to 2.5 for  $\alpha_{eq} = 90^\circ$   
 425 (Baumjohann and Treumann, 1997). Since the rate of adiabatic heating is greater in  
 426 the perpendicular direction than heating in the parallel direction, an initially isotropic  
 427 particle distribution will become anisotropic during its convection. These isotropic  
 428 particles can then become unstable to wave growth and generate waves in order to  
 429 reach equilibrium.

430 Wave Resonance Heating

431 Another mechanism that heats particles is due to particles resonating with  
 432 plasma waves. A few of the electromagnetic wave modes responsible for particle  
 433 acceleration (and deceleration) relevant to radiation belt dynamics are hiss, whistler  
 434 mode chorus (chorus), and electromagnetic ion cyclotron (EMIC) waves. These waves  
 435 are created by the loss cone instability that driven by an anisotropy of electrons  
 436 for chorus waves, and protons for EMIC waves. The level of anisotropy can be  
 437 quantified by the ratio of the perpendicular to parallel particle temperatures ( $T_\perp/T_{||}$ ).  
 438 A particle distribution is unstable when  $T_\perp/T_{||} > 1$  which facilitates wave growth.  
 439 Since electrons gyrate in a right-handed sense, the chorus waves also tend to be right  
 440 hand circularly polarized (Tsurutani and Lakhina, 1997). The same argument applies  
 441 to protons and left hand circularly polarized EMIC waves as well.

442 These circularly polarized waves can resonate with electrons and/or protons  
 443 when their combined motion results in a static  $\vec{E}$ . One example of a resonance  
 444 between a right hand circularly polarized wave and an electron is shown in Fig. 1.21  
 445 and is termed the cyclotron resonance. An electron's  $v_{||}$  and the wave's parallel wave  
 446 vector,  $k_{||}$  are in opposite directions such that the wave frequency  $\omega$  is Doppler shifted  
 447 to an integer multiple of the  $\Omega_e$  at which point the electron feels a static electric  
 448 field and is accelerated or decelerated. This acceleration happens when a resonance



$$\omega + \mathbf{k}_{\parallel} \mathbf{V}_{\parallel} = \Omega^-$$

Figure 1.11: The trajectories of an electron and a right-hand circularly polarized wave during a cyclotron resonance. The electron's  $v_{\parallel}$  and the wave's  $k_{\parallel}$  are in opposite directions such that the wave's frequency is Doppler shifted to an integer multiple of the electron cyclotron frequency. Figure from (Tsurutani and Lakhina, 1997).

449 condition is satisfied between a wave and a particle for which we will now derive an  
450 illustrative toy model.

451 Assume a uniform magnetic field  $\vec{B} = B_0 \hat{z}$  with a parallel propagating ( $k = k \hat{z}$ ),  
452 right-hand circularly polarized wave. The wave's electric field as a function of position  
453 and time can be written as

$$\vec{E} = E_0 (\cos(\omega t - kz) \hat{x} + \sin(\omega t - kz) \hat{y}) \quad (1.16)$$

which is more clearly expressed by taking the dot product to find  $\vec{E}$  in the  $\hat{\theta}$  direction

$$E_{\theta} = \vec{E} \times \hat{\theta} = E_0 \cos(\omega t - kz + \theta). \quad (1.17)$$

454 Now assume that the electron is traveling in the  $-\hat{z}$  direction with a velocity  $\vec{v} = -v_0 \hat{z}$   
455 so its time dependent position along  $\hat{z}$  is

$$z(t) = -v_0 t \quad (1.18)$$

456 and gyrophase is

$$\theta(t) = -\Omega t + \theta(0) \quad (1.19)$$

457 where the first negative sign comes from the electron's negative charge. Now we put  
458 this all together and express the electric field and the force that the electron will  
459 experience

$$m \frac{dv_\theta}{dt} = qE_\theta = qE_0 \sin((\omega + kv_0 - \Omega)t + \theta(0)). \quad (1.20)$$

460 This is a relatively complex expression, but when the time dependent component,

$$\omega + kv_0 - \Omega = 0, \quad (1.21)$$

461 the electron will be in a static electric field which will accelerate or decelerate the  
462 electron depending on  $\theta_0$ , the phase between the wave and the electron. **Show Bortnik**  
463 **2008 plot?** The expression in Eq. 1.21 is commonly referred to as the resonance  
464 condition and is more generally written as

$$\omega - k_{||}v_{||} = \frac{n\Omega_e}{\gamma} \quad (1.22)$$

465 where  $n$  is the resonance order, and  $\gamma$  is the relativistic correction (e.g. Millan and  
466 Thorne, 2007). In the case of the cyclotron resonance,  $\omega \approx \Omega_e$  thus  $J_1$  is violated.  
467 Since  $J_1$  is violated,  $J_2$  and  $J_3$  are also violated since the conditions required to  
468 violate  $J_2$  and  $J_3$  are less stringent than  $J_1$ . It is important to remember that along  
469 the particle's orbit it will encounter and experience the effects of many waves along  
470 its orbit. The typical MLT extent of a handful of waves that are capable of resonating  
471 with radiation belt electrons are shown in Fig. 1.12.

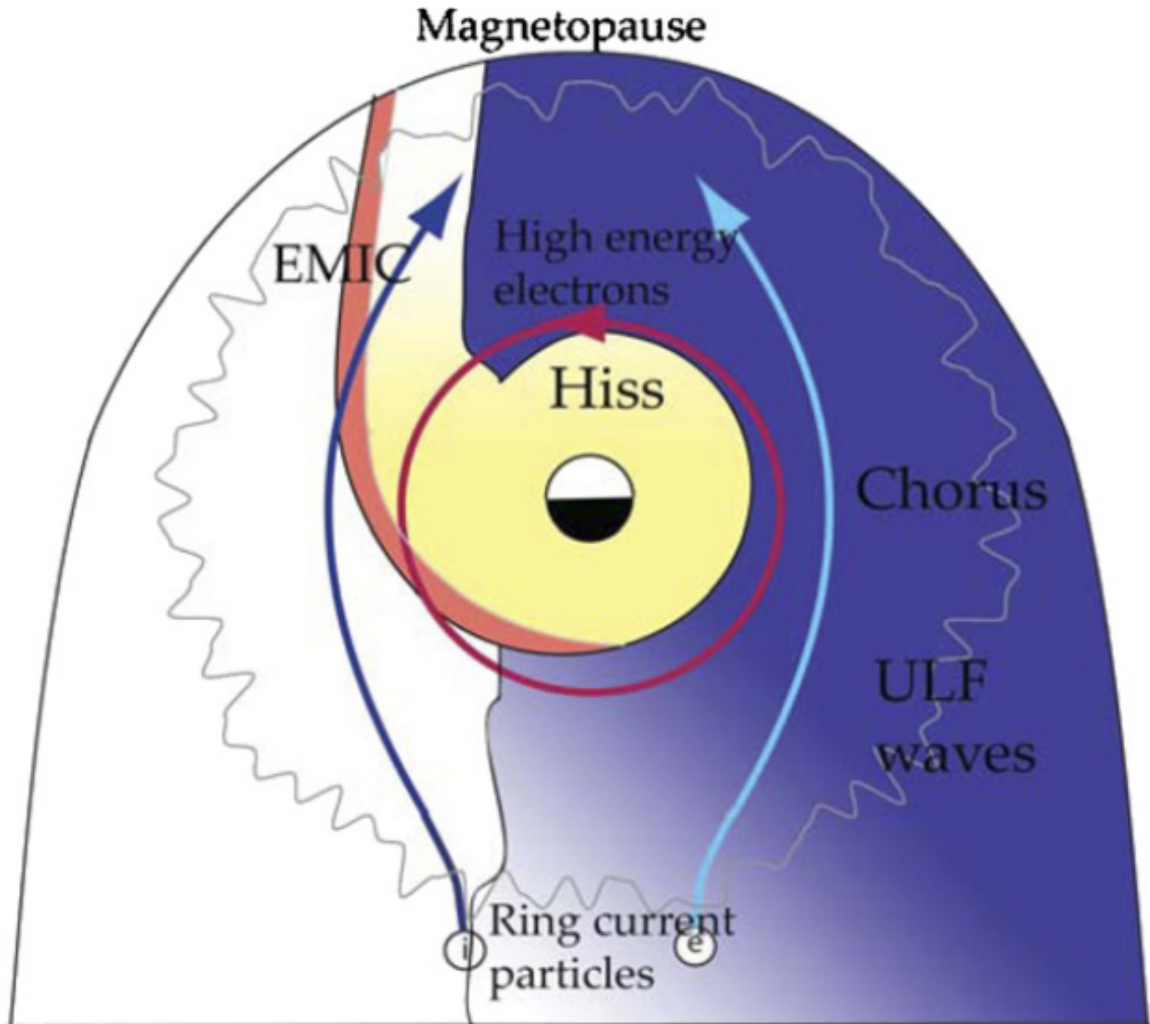


Figure 1.12: Various wave modes in the magnetosphere. Ultra low frequency waves occur through the magnetosphere. Chorus waves are typically observed in the 0-12 midnight-dawn region. EMIC waves are typically observed in the dusk MLT sector. Hiss waves are observed inside the plasmasphere. Figure from Millan and Thorne (2007).

472 Particle Losses

473 Now that we have seen two general mechanisms with which particles are  
 474 accelerated and transported in the magnetosphere, we will now consider a few  
 475 specific mechanisms with which particles are lost to the atmosphere or the solar  
 476 wind. One particle loss mechanism into the solar wind is magnetopause shadowing  
 477 (e.g. Ukhorskiy et al., 2006). Particles are sometimes lost when the ring current is  
 478 strengthened and Earth's magnetic field strength is increased outside of the ring  
 479 current (and reduced on Earth's surface). If the time scale of the ring current  
 480 strengthening is slower than a particle drift,  $J_3$  is conserved. Then in order to  
 481 conserve  $J_3$  while the magnetic field strength is increased, the particle's drift shell  
 482 must move outward to conserve the magnetic flux contained by the drift shell. Then  
 483 if the particle's drift shell expands to the point that it crosses the magnetopause, the  
 484 particle will be lost to the solar wind.

485 **Move to acceleration?** Another particle loss and acceleration mechanism is driven  
 486 by ultra low frequency (ULF) waves and is called radial diffusion. Radial diffusion is  
 487 the transport of particles from high to low phase space density,  $f$ . If the transport is  
 488 radially inward, particles will appear to be accelerated. On the other hand, radially  
 489 outward radial diffusion can transport particles through the magnetopause where  
 490 they will be lost to the solar wind. Reeves et al. (2013) investigated the driver of  
 491 particle acceleration during the October 2012 storm and observationally found that  
 492 inward radial diffusion was not dominant, rather local acceleration via wave-resonance  
 493 heating (i.e. particle diffusion in pitch angle and energy which will be described below)  
 494 appeared to be the dominant acceleration mechanism.

495 The loss mechanism central to this dissertation is pitch angle and energy  
 496 scattering of electrons by waves. Some of the waves that scatter electrons in energy  
 497 and pitch angle in the inner magnetosphere are: plasmaspheric hiss (e.g. Breneman

498 et al., 2015; O'Brien et al., 2014), EMIC waves (e.g. Capannolo et al., 2019; Hendry  
 499 et al., 2017), and chorus waves (e.g. Breneman et al., 2017; Kasahara et al., 2018;  
 500 Ozaki et al., 2019). These wave-particle interactions occur when the resonance  
 501 condition in Eq. 1.22 is satisfied at which point the particle's energy and  $\alpha$  is modified  
 502 by the wave. More details regarding the theory of pitch angle and energy diffusion is  
 503 given in Chapter X. If the wave changes  $\alpha$  towards 0 such that  $\alpha < \alpha_{LC}$ , the particle's  
 504 mirror point lowers to less than 100 km altitude where the particle can be lost due  
 505 collisions with air. One manifestation of pitch angle scattering of particles into the  
 506 loss cone are microbursts: a sub-second durtaison impulse of electrons.

507

### Microbursts

508 Microbursts were first identified in high altitude balloon observations of bremsstrahlung  
 509 X-rays emitted by microburst electrons impacting the atmosphere by Anderson and  
 510 Milton (1964). Since then, other balloons have observed microburst X-ray signatures  
 511 in the upper atmosphere (e.g. Anderson et al., 2017; Barcus et al., 1966; Brown et al.,  
 512 1965; Parks, 1967; Trefall et al., 1966; Woodger et al., 2015). In addition to their X-ray  
 513 signature, microbursts electrons have been directly observed in LEO with spacecraft  
 514 including the Solar Anomalous and Magnetospheric Particle Explorer (SAMPEX),  
 515 Focused Investigation of Relativistic Electron Bursts: Intensity, Range, and Dynamics  
 516 II (FIREBIRD-II), Science Technologies Satellite (STSAT-I) (e.g. Blake et al., 1996;  
 517 Blum et al., 2015; Breneman et al., 2017; Crew et al., 2016; Lee et al., 2012, 2005;  
 518 Lorentzen et al., 2001a,b; Nakamura et al., 1995, 2000; O'Brien et al., 2004, 2003).  
 519 An example microburst time series is shown in Fig. 1.13 and was observed by  
 520 Montana State University's (MSU) FIREBIRD-II CubeSats. The prominent features  
 521 of microbursts in Fig. 1.13 are their  $\pm 1$  second duration, half order of magnitude  
 522 increase in count rate above the falling background, and their approximately 200-800

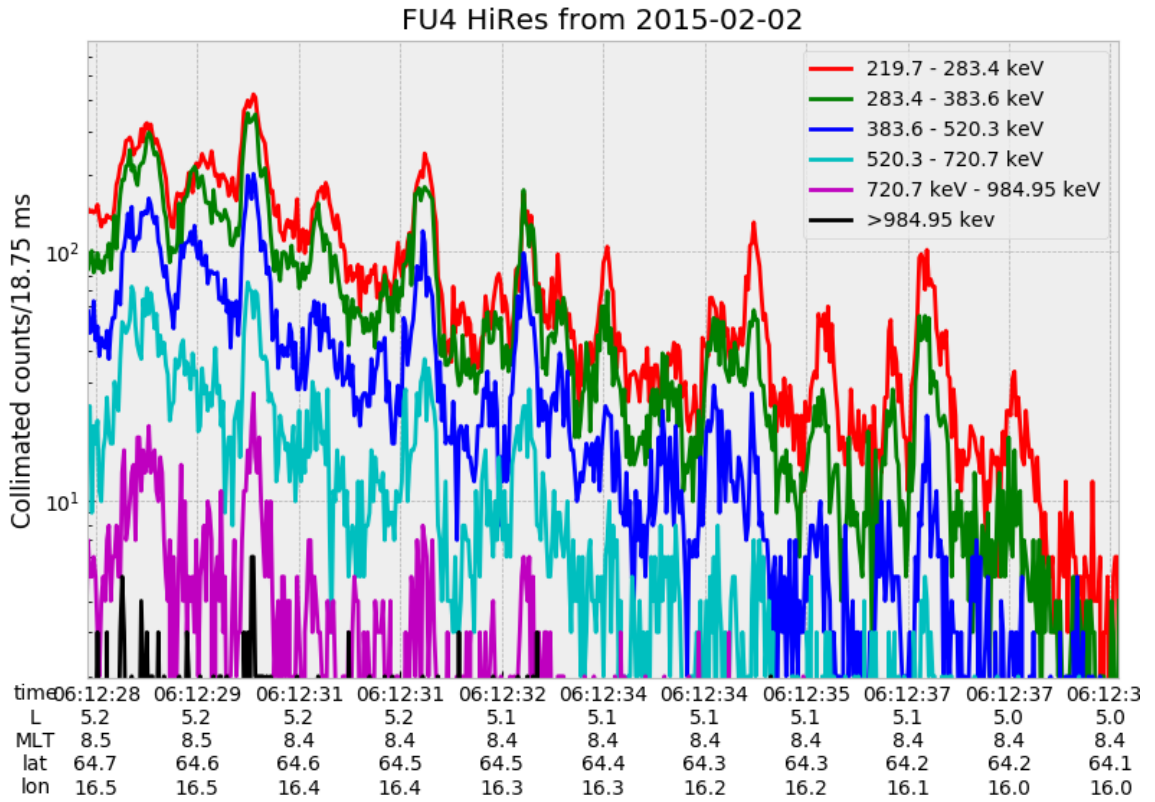


Figure 1.13: An example train of microbursts observed by FIREBIRD-II unit 4 on February 2nd, 2015. The colored curves show the differential energy channel count rates in six channels from  $\approx 200$  keV to greater than 1 MeV. The x-axis labels show auxiliary information such as time of observation and the spacecraft position in L, MLT, latitude and longitude coordinates.

523 keV energy extent.

524 Microbursts are observed on magnetic field footprints that are connected to the  
 525 outer radiation belt (approximately  $4 < L < 8$ ), and are predominately observed in  
 526 the 0-12 MLT sector with an elevated occurrence frequency during magnetospherically  
 527 disturbed times as shown in Fig. 1.14. Microbursts have been previously observed  
 528 over a wide energy range from a few tens of keV (Datta et al., 1997; Parks, 1967) to  
 529 greater than 1 MeV (e.g. Blake et al., 1996; Greeley et al., 2019). The microburst

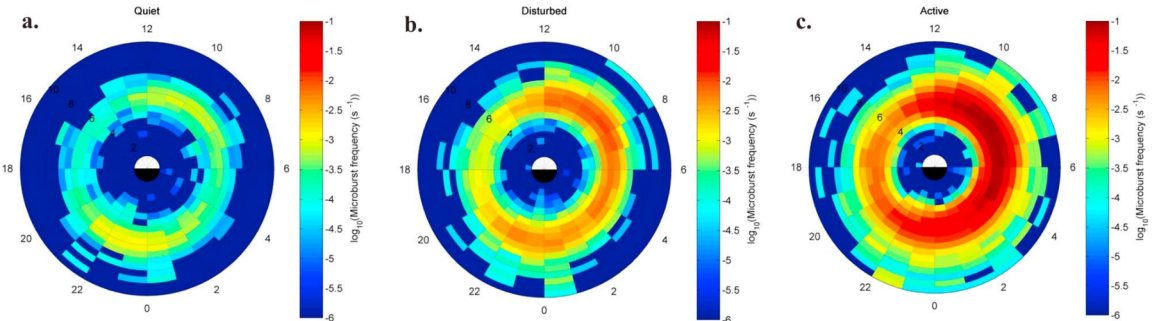


Figure 1.14: Relativistic ( $> 1\text{MeV}$ ) distribution of microburst occurrence rates as a function of  $L$  and MLT. The three panels show the microburst occurrence rate dependence on geomagnetic activity, parameterized by the auroral electrojet (AE) index for (a)  $\text{AE} < 100 \text{ nT}$ , (b)  $100 < \text{AE} < 300 \text{ nT}$  and (c)  $\text{AE} > 300 \text{ nT}$ . Figure from Douma et al. (2017).

530 electron flux ( $J$ ) falls off in energy, and the microburst energy spectra is typically  
 531 well fit to a decaying exponential

$$J(E) = J_0 e^{-E/E_0} \quad (1.23)$$

532 where  $J_0$  is the flux at 0 keV (unphysical free parameter) and  $E_0$  quantifies the  
 533 efficiency of the scattering mechanism in energy (.e.g Datta et al., 1997; Lee et al.,  
 534 2005; Parks, 1967). A small  $E_0$  suggests that mostly low energy particles are scattered  
 535 and a high  $E_0$  suggests that the scattering mechanism scatters low and high energy  
 536 electrons. Reality is a bit more messy and a high  $E_0$  may be a signature of a scattering  
 537 mechanism preferential to high energy electrons, but is hidden by the convolution of  
 538 the source particles available to be scattered (typically with a falling energy spectrum)  
 539 and the energy-dependent scattering efficiency.

540 The short duration of microbursts observed by a single LEO satellite has an  
 541 ambiguity when interpreting what is exactly a microburst. The two possible realities  
 542 are: a microburst is very small and spatially stationary so that the LEO spacecraft

543 passes through it in less than a second. Alternatively, microbursts are spatially large  
 544 with a short duration such that the microburst passes by the spacecraft in a fraction  
 545 of a second. There are a few ways to distinguish between the two possible realities,  
 546 and each one has a unique set of advantages.

547 A high altitude balloon provides essentially a stationary view of the precipitating  
 548 particles under the radiation belt footprints so a short-lived, temporal microburst  
 549 can be unambiguously identified. Spatial structures on the other hand are difficult  
 550 to identify because a balloon is essentially still on drift timescales thus a variation in  
 551 the X-rays can be due to the spatial structure or an increase of precipitating particles  
 552 over the whole area. Furthermore, if the stationary structure is drifting its particles  
 553 are not precipitating into the atmosphere so there is no X-ray signature.

554 Another solution is multi-spacecraft missions that can determine if a microburst  
 555 is spatial or temporal. As will be shown in this dissertation, if a microburst is  
 556 observed simultaneously by two spacecraft then it is temporally transient and has  
 557 a size greater than the spacecraft separation. On the other hand, if two spacecraft  
 558 observe a microburst-like feature in the same location and at different times, then it is  
 559 spatial may be a curtain (Blake and O'Brien, 2016). Both observational methods have  
 560 a unique set of strengths, and this dissertation takes the multi-spacecraft approach  
 561 to identify and study microbursts.

562

### Scope of Research

563 This dissertation furthers our understanding of the microburst scattering  
 564 mechanism by observing the scattering directly, and measuring the microburst sizes  
 565 and comparing them to the size of waves near the magnetic equator where those  
 566 electrons could have been scattered. Chapter X describes a microburst scattering  
 567 event observed by NASA's Van Allen Probes which was studied in the theoretic

568 framework of pitch angle and energy diffusion. The following two chapters will then  
569 study the size of microbursts. Chapter Y describes a bouncing packet microburst  
570 observation made by MSU's FIREBIRD-II mission where the microburst's lower  
571 bound longitudinal and latitudinal sizes were estimated. Then Chapter Z expands  
572 the case study from Ch. Y to a statistical study of microburst sizes using The  
573 Aerospace Corporation's AeroCube-6 (AC6) CubeSats. In this study, a Monte Carlo  
574 and analytic microburst size models were developed to account for the compounding  
575 effects of random microburst sizes and locations. Lastly, Ch. A will summarize the  
576 dissertation work and make concluding remarks regarding outstanding questions in  
577 microburst physics.

## 578 CHAPTER THREE

579 MICROBURST SCALE SIZE DERIVED FROM MULTIPLE BOUNCES OF A  
580 MICROBURST SIMULTANEOUSLY OBSERVED WITH THE FIREBIRD-II  
581 CUBESATS

582 Contribution of Authors and Co-Authors

583 Manuscript(s) in Chapter(s) 1

584

585 Author: [type author name here]

586 Contributions: [list contributions here, single-spaced]

587 Co-Author: [type co-author name here]

588 Contributions: [list contributions here, single-spaced]

589 Co-Author: [type co-author name here]

590 Contributions: [list contributions here, single-spaced]

591

592

Manuscript Information

593 [Type Author and Co-author(s) Names Here]

594 Geophysical Research Letters

595 Status of Manuscript: Published in a peer-reviewed journal

596 Wiley

597 Volume 45, Issue 17

598

Key Points

- 599     • Multiple bounces from a microburst were observed by the two FIREBIRD-II  
 600           CubeSats at LEO.
- 601     • The lower bounds on the microburst scale size at LEO were  $29 \pm 1$  km  
 602           (latitudinal) and  $51 \pm 11$  km (longitudinal).
- 603     • Deduced lower bound equatorial scale size was similar to the whistler-mode  
 604           chorus source scale.

605

Abstract

606     We present the observation of a spatially large microburst with multiple bounces  
 607     made simultaneously by the FIREBIRD-II CubeSats on February 2nd, 2015. This  
 608     is the first observation of a microburst with a subsequent decay made by two co-  
 609     orbiting but spatially separated spacecraft. From these unique measurements, we  
 610     place estimates on the lower bounds of the spatial scales as well as quantify the  
 611     electron bounce periods. The microburst's lower bound latitudinal scale size was  
 612      $29 \pm 1$  km and the longitudinal scale size was  $51 \pm 1$  km in low earth orbit. We  
 613     mapped these scale sizes to the magnetic equator and found that the radial and  
 614     azimuthal scale sizes were at least  $500 \pm 10$  km and  $530 \pm 10$  km, respectively. These  
 615     lower bound equatorial scale sizes are similar to whistler-mode chorus wave source  
 616     scale sizes, which supports the hypothesis that microbursts are a product of electron  
 617     scattering by chorus waves. Lastly, we estimated the bounce periods for 200-800 keV  
 618     electrons and found good agreement with four common magnetic field models.

619

Introduction

620       The dynamics of radiation belt electrons are complex, and are driven by  
 621 competition between source and loss processes. A few possible loss processes are  
 622 radial diffusion (Shprits and Thorne, 2004), magnetopause shadowing (Ukhorskiy  
 623 et al., 2006), and pitch angle and energy diffusion due to scattering of electrons by  
 624 plasma waves (e.g. Abel and Thorne, 1998; Horne and Thorne, 2003; Meredith et al.,  
 625 2002; Mozer et al., 2018; Selesnick et al., 2003; Summers et al., 1998; Thorne et al.,  
 626 2005). There are a variety of waves that cause pitch angle scattering, including  
 627 electromagnetic ion cyclotron waves, plasmaspheric hiss, and chorus (Millan and  
 628 Thorne, 2007; Thorne, 2010). Chorus predominantly occurs in the dawn sector (6-  
 629 12 magnetic local times (MLT)) (Li et al., 2009) where it accelerates electrons with  
 630 large equatorial pitch angles and scatters electrons with small equatorial pitch angles  
 631 (Horne and Thorne, 2003). Some of these electrons may be impulsively scattered  
 632 into the loss cone, where they result in short-duration ( $\sim 100$  ms) enhancements in  
 633 precipitating flux called microbursts.

634       Anderson and Milton (1964) coined the term microburst to describe high altitude  
 635 balloon observations of  $\sim 100$  ms duration enhancements of bremsstrahlung X-  
 636 rays emitted from scattered microburst electrons impacting the atmosphere. Since  
 637 then, non-relativistic (less than a few hundred keV) microbursts have been routinely  
 638 observed with other balloon missions (e.g. Anderson et al., 2017; Parks, 1967; Woodger  
 639 et al., 2015). A review of the literature shows no reports of microbursts above a few  
 640 hundred keV observed by balloons (Millan et al., 2002; Woodger et al., 2015). This  
 641 lack of observation may be explained by relatively weaker pitch angle scattering of  
 642 relativistic electrons by chorus (Lee et al., 2012).

643       In addition to the X-ray signature for bursts of electron precipitation, the

644 precipitating relativistic and non-relativistic electrons have been measured in situ by  
 645 spacecraft orbiting in low earth orbit (LEO). Hereinafter, we refer to these electron  
 646 signatures observed by LEO spacecraft also as microbursts. Microbursts have been  
 647 observed with, e.g. the Solar Anomalous and Magnetospheric Particle Explorer's  
 648 (SAMPEX)  $\gtrsim$  150 keV and  $\gtrsim$  1 MeV channels (Blake et al., 1996; Blum et al., 2015;  
 649 Lorentzen et al., 2001a,b; Nakamura et al., 1995, 2000; O'Brien et al., 2004, 2003) and  
 650 Focused Investigation of Relativistic Electron Bursts: Intensity, Range, and Dynamics  
 651 (FIREBIRD-II) with its  $\gtrsim$  200 keV energy channels (Anderson et al., 2017; Breneman  
 652 et al., 2017; Crew et al., 2016).

653 Understanding microburst precipitation and its scattering mechanism is impor-  
 654 tant to radiation belt dynamics. The scattering mechanism has been observationally  
 655 studied by e.g. Lorentzen et al. (2001b) who found that microbursts and chorus  
 656 waves predominantly occur in the dawn sector and Breneman et al. (2017) made  
 657 a direct observational link between individual microbursts and chorus elements.  
 658 Microbursts have been modeled and empirically estimated to be capable of depleting  
 659 the relativistic electron population in the outer radiation belt on the order of a day  
 660 (Breneman et al., 2017; O'Brien et al., 2004; Shprits et al., 2007; Thorne et al., 2005).  
 661 An important parameter in this estimation of instantaneous radiation belt electron  
 662 losses due to microbursts is their scale size. Parks (1967) used balloon measurements  
 663 of bremsstrahlung X-rays to estimate the high altitude scale size of predominantly low  
 664 energy microbursts to be  $40 \pm 14$  km. In Blake et al. (1996) a microburst with multiple  
 665 bounces was observed by SAMPEX, and the microburst's latitudinal scale size in LEO  
 666 was estimated to have been "at least a few tens of kilometers". Blake et al. (1996)  
 667 concluded that typically microbursts are less than a few tens of electron gyroradii in  
 668 size (at  $L = 5$  at LEO, the gyroradii of 1 MeV electrons is on the order of 100 m).  
 669 Dietrich et al. (2010) used SAMPEX along with ground-based very low frequency

670 stations to conclude that during one SAMPEX pass, the observed microbursts had  
671 scale sizes less than 4 km.

672 Since February 1st, 2015, microbursts have been observed by FIREBIRD-II, a  
673 pair of CubeSats in LEO. Soon after launch, when the two FIREBIRD-II spacecraft  
674 were at close range, a microburst with a scale size greater than 11 km was observed  
675 (Crew et al., 2016). On the same day, FIREBIRD-II simultaneously observed a  
676 microburst with multiple bounces. The microburst decay was observed over a period  
677 of a few seconds, while the spacecraft were traveling predominantly in latitude. Here  
678 we present the analysis and results of the latitude and longitude scale sizes and  
679 bounce periods of the first microburst with multiple bounces observed with the two  
680 FIREBIRD-II spacecraft.

681

### Spacecraft and Observation

682 The FIREBIRD missions are comprised of a pair of identically-instrumented  
683 1.5U CubeSats (15 x 10 x 10 cm) that are designed to measure electron precipitation  
684 in LEO (Klumpar et al., 2015; Spence et al., 2012). The second mission, termed  
685 FIREBIRD-II, was launched on January 31st 2015. The two FIREBIRD-II CubeSats,  
686 identified as Flight Unit 3 (FU3) and Flight Unit 4 (FU4), were placed in a 632 km  
687 apogee, 433 km perigee, and 99° inclination orbit (Crew et al., 2016). FU3 and FU4  
688 are orbiting in a string of pearls configuration with FU4 ahead, to resolve the space-  
689 time ambiguity of microbursts. Each FIREBIRD-II unit has two solid state detectors:  
690 one is mounted essentially at the spacecraft surface, covered only by a thin foil acting  
691 as a sun shade, with a field of view of 90° (surface detector), and the other is beneath  
692 a collimator which restricts the field of view to 54° (collimated detector). Only FU3  
693 has a functioning surface detector, so this analysis utilizes the collimated detectors.  
694 FU3's surface and collimated detectors, as well as FU4's collimated detector observe

695 electron fluxes in six energy channels from  $\sim 230$  keV to  $> 1$  MeV. FIREBIRD-II's  
 696 High Resolution (HiRes) electron flux data is gathered with an adjustable sampling  
 697 period of 18.75 ms by default and can be as fast as 12.5 ms.

700 On February 2nd, 2015 at 06:12 UT, both FIREBIRD-II spacecraft simultaneously observed an initial microburst, followed by subsequent periodic electron  
 701 enhancements of diminishing amplitude shown in Fig. 2.1. This is thought to be  
 702 the signature of a single burst of electrons, some of which precipitate, but the rest  
 703 mirror near the spacecraft then bounce to the conjugate hemisphere where they mirror  
 704 again and the subsequent bounces produce a train of decaying peaks (Blake et al.,  
 705 1996; Thorne et al., 2005). This bounce signature occurred during the transition  
 706 between the main and recovery phases of a storm with a minimum Dst of -44 nT  
 707 ( $K_p = 4$ , and  $AE \approx 400$  nT). At this time, the HiRes data was sampled at 18.75 ms.  
 708 Five peaks were observed by both spacecraft. The fifth peak observed by FU4 was  
 709 comparable to the Poisson noise and was not used in this analysis. This microburst  
 710 was observed from the first energy channel ( $\approx 200 - 300$  keV), to the fourth energy  
 711 channel ( $\approx 500 - 700$  keV), and FU3's surface detector observed the microburst up  
 712 to the fifth energy channel (683 - 950 keV).

713 The HiRes data in Fig. 2.1 shows signs of energy dispersion, characterized by  
 714 higher energy electrons arriving earlier than the lower energies. This time of flight  
 715 energy dispersion tends to smear out the initial sharp burst upon each subsequent  
 716 bounce. The first peak does not appear to be dispersed, and subsequent peaks show  
 717 a dispersion trend consistent across energy channels. The black vertical bars have  
 718 been added to Fig. 2.1 to highlight this energy dispersion. This dispersion signature  
 719 and amplitude decay implies that the first peak was observed soon after the electrons  
 720 were scattered, followed by decaying bounces.

At this time, in magnetic coordinates, FIREBIRD-II was at McIlwain  $L = 4.7$

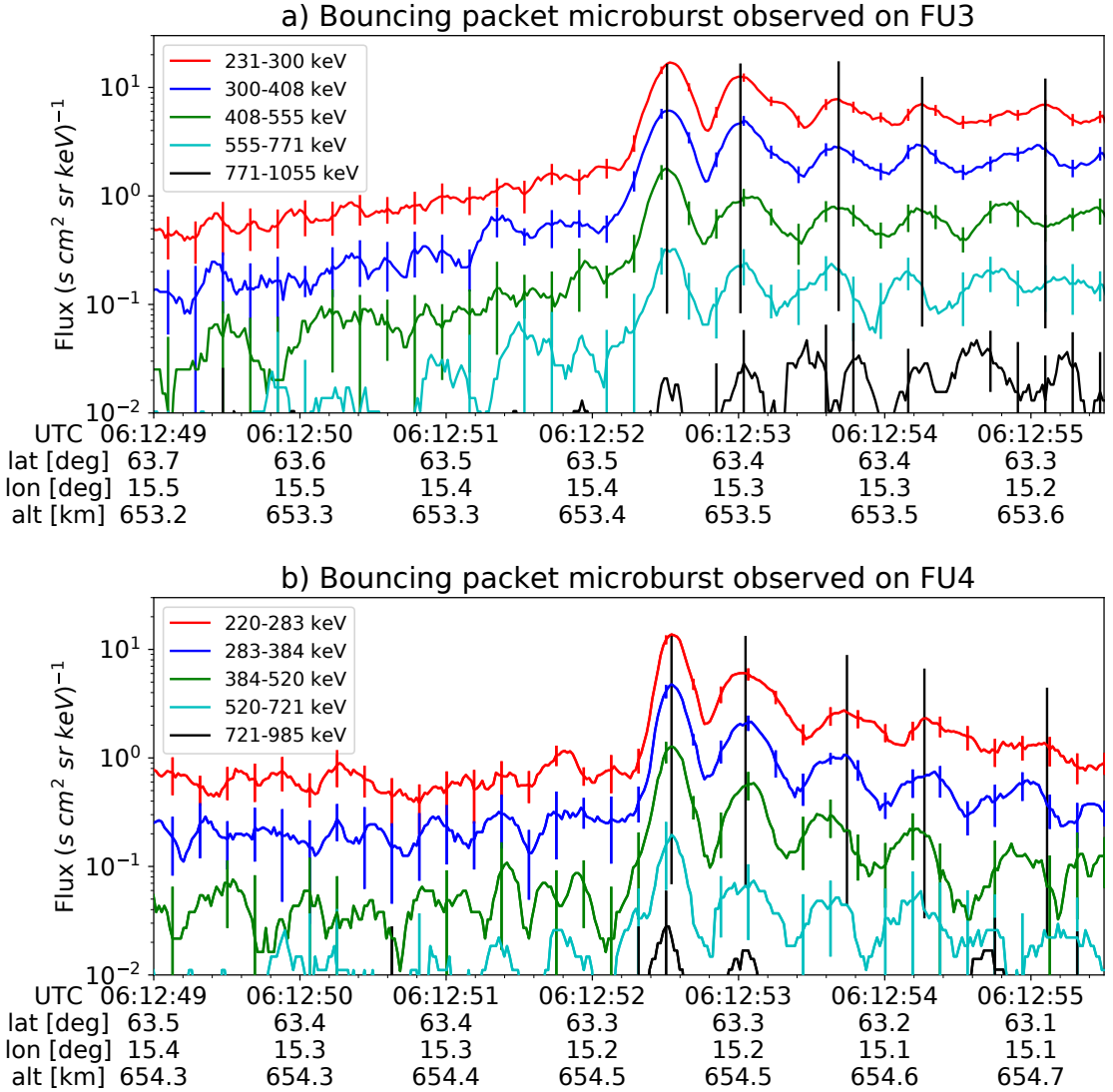


Figure 2.1: HiRes data of the microburst observed at February 2nd, 2015 at 06:12:53 UT, smoothed with a 150 ms rolling average. The subsequent bounces showed some energy dispersion. As discussed in Appendix A, a time correction of -2.28 s was applied to FU3. While the flux from five energy channels is shown, only channels with reasonable counting statistics were used for the spatial scale analysis. Vertical colored bars show the  $\sqrt{N}$  error every 10th data point and vertical black bars are lined up with the peaks in the 220-283 keV energy channel to help identify dispersion.

and MLT = 8.3, calculated with the Tsyganenko 1989 (T89) magnetic field model (Tsyganenko, 1989) using IRBEM-Lib (Boscher et al., 2012). Geographically, they were above Sweden, latitude = 63°N, longitude = 15°E, altitude = 650 km. This geographic location is magnetically conjugate to the east of the so-called South Atlantic Anomaly (SAA). The SAA is the location where the mirror points of electrons tend to occur at locations deeper in the atmosphere owing to the offset of the dipole magnetic field from the Earth's center. Electrons with pitch angles within the drift loss cone (DLC) will encounter the SAA and be removed from their eastward longitudinal drift paths (Comess et al., 2013; Dietrich et al., 2010). FU3 and FU4 are therefore both in regions where the particles in the DLC have recently precipitated, leaving only particles that were recently scattered. At the spacecraft location, locally mirroring electrons would have mirrored at 95 km in the opposite hemisphere, with more field aligned electrons mirroring at even lower altitudes. From the analysis done by Fang et al. (2010), the peak in the total ionization rate in the atmosphere for 100 keV electrons is around 80 km altitude, while the total ionization rate from 1 MeV electrons peaks around 60 km altitude. It is, therefore, expected that a fraction of the microburst electrons will survive each encounter with the atmosphere. By plotting the peak flux as a function of bounce (not shown), it was found that 40 - 60 % of the microburst electrons were lost on the first bounce, similar to the 33% loss per bounce observed for a bouncing microburst observed by SAMPEX (Thorne et al., 2005).

741

### Analysis

At the beginning of the FIREBIRD-II mission, two issues prevented the proper analysis of the microburst's spatial scale size: the spacecraft clocks were not synchronized, and their relative positions were not accurately known. We addressed these issues with a cross-correlation time lag analysis described in detail in Appendix

<sup>746</sup> A. From this analysis, the time correction was  $2.28 \pm 0.12$  s (applied to Fig. 2.1) and  
<sup>747</sup> the separation was  $19.9 \pm 0.9$  km at the time of the microburst observation.

<sup>748</sup> Electron Bounce Period

<sup>749</sup> We used this unique observation of bouncing electrons to calculate the bounce  
<sup>750</sup> period,  $t_b$  as a function of energy and compare it to the energy-dependent  $t_b$  curves  
<sup>751</sup> derived from four magnetic field models, the results of which are shown in Fig. 2.2.  
<sup>752</sup> The observed  $t_b$  and uncertainties were calculated by fitting the baseline-subtracted  
<sup>753</sup> HiRes flux. The baseline flux used in this analysis is given in O'Brien et al. (2004)  
<sup>754</sup> as the flux at the 10th percentile over a specified time interval, which in this analysis  
<sup>755</sup> was taken to be 0.5 seconds. The flux was fitted with a superposition of Gaussians  
<sup>756</sup> for each energy channel, and the uncertainty in flux was calculated using the Poisson  
<sup>757</sup> error from the microburst and baseline fluxes summed in quadrature. Using the fit  
<sup>758</sup> parameters, the mean  $t_b$  for the lowest four energy channels is shown in Fig. 2.2. The  
<sup>759</sup> trend of decreasing  $t_b$  as a function of energy is evident in Fig. 2.2, which further  
<sup>760</sup> supports the assumption that the subsequent peaks are bounces, and not a train of  
<sup>761</sup> microbursts scattered by bouncing chorus.

<sup>762</sup> The decaying peaks in the 231-408 keV electron flux observed by FU3's lowest  
<sup>763</sup> two energy channels (see Fig. 2.1) were right-skewed. One explanation is that there  
<sup>764</sup> was in-channel energy dispersion within those channels. Since  $t_b$  of higher energy  
<sup>765</sup> electrons is shorter, a right-skewed peak implies that higher energy electrons were  
<sup>766</sup> more abundant within that channel e.g. in FU3's 231-300 keV channel, the 300 keV  
<sup>767</sup> electrons will arrive sooner than the 231 keV electrons, but will they will be binned  
<sup>768</sup> in the same channel. A Gaussian fit cannot account for this in-channel dispersion,  
<sup>769</sup> and as a first order correction, minima between peaks was used to calculate  $t_b$ , and  
<sup>770</sup> is shown in Fig. 2.2. The observed energy-dependent dispersion shown in Fig. 2.2

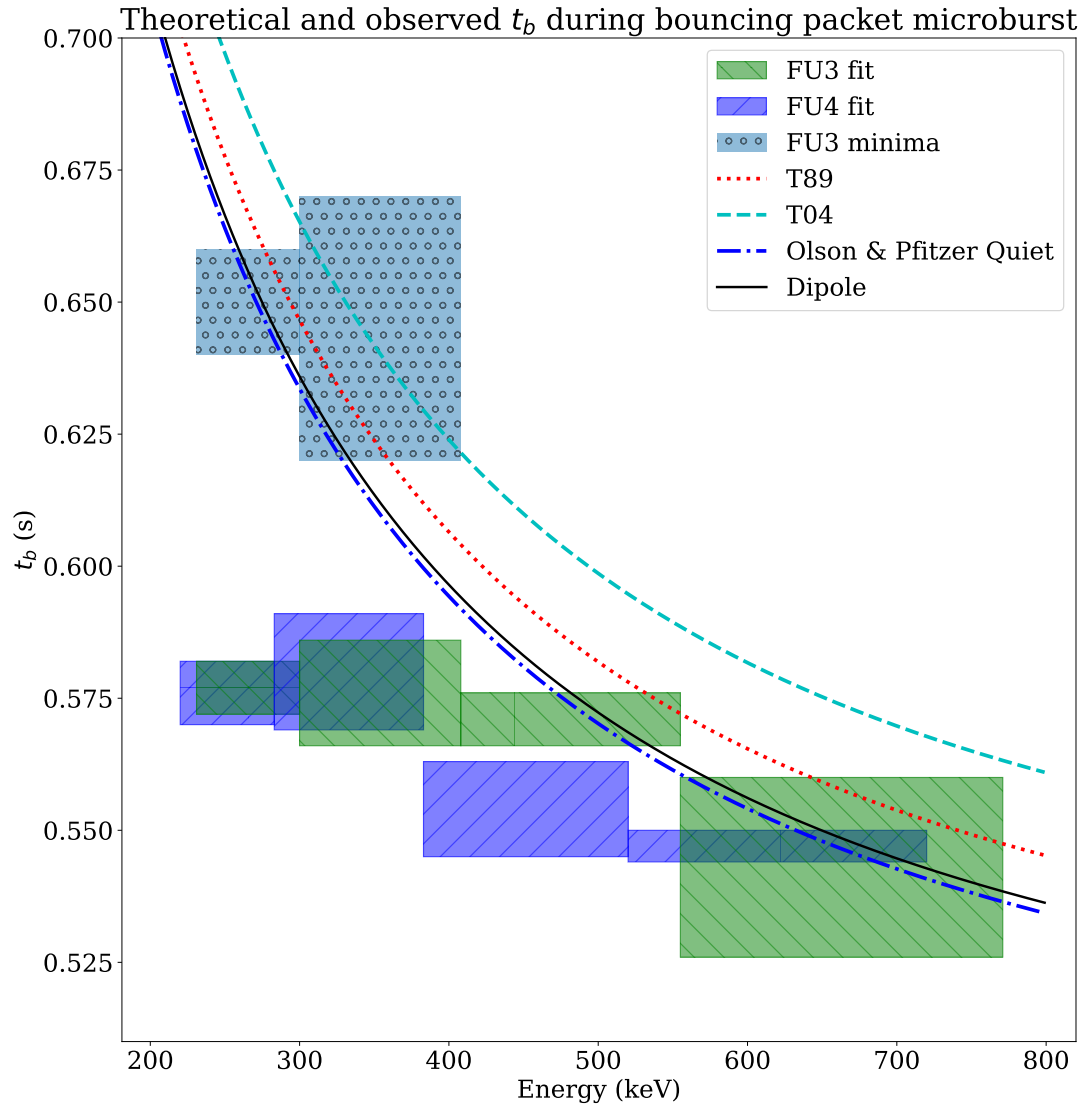


Figure 2.2: Observed and theoretical  $t_b$  for electrons of energies from 200 to 770 keV. The solid black line is  $t_b$  in a dipole magnetic field, derived in Schulz and Lanzerotti (1974). The red dotted and cyan dashed lines are the  $t_b$  derived using the T89, and T04 magnetic field models with IRBEM-Lib. Lastly, the blue dot-dash curve is the  $t_b$  derived using the Olson & Pfitzer Quiet model. The green and purple rectangles represent the observed  $t_b$  for FU3 and FU4 using a Gaussian fit, respectively. The blue rectangles represent the observed  $t_b$  calculated with the minima between the bounces. The width of the boxes represent the width of those energy channels, and the height represents the uncertainty from the fit.

771 is consistent with higher energy peaks returning sooner. This dispersion consistency  
 772 further supports the assumption that the subsequent peaks are bounces, and not a  
 773 train of microbursts scattered by bouncing chorus.

774 To compare the observed and modeled  $t_b$ , we superposed  $t_b$  curves for various  
 775 models including an analytical solution in a dipole (Schulz and Lanzerotti, 1974), and  
 776 numerical models: T89, Tsyganenko 2004 (T04) (Tsyganenko and Sitnov, 2005), and  
 777 Olson & Pfitzer Quiet (Olson and Pfitzer, 1982) in Fig. 2.2. The numerical  $t_b$  curves  
 778 were calculated using a wrapper for IRBEM-Lib. This code traces the magnetic field  
 779 line between mirror points, and calculates  $t_b$  assuming conservation of energy and the  
 780 first adiabatic invariant for electrons mirroring at FIREBIRD-II. With the empirical  
 781  $t_b$ , the models agree within FIREBIRD-II's uncertainties, but the T04 model has the  
 782 largest discrepancy compared to the other models.

### 783 Microburst Energy Spectra

784 Next, we investigated the energy spectra of this microburst. The energy spectra  
 785 was modeled with an exponential that was fit to the peak flux derived from the  
 786 Gaussian fit parameters in section 2 to all but the highest energy channel. We found  
 787 that the E-folding energy,  $E_0 \sim 100$  keV. This spectra is similar to spectra show  
 788 by Lee et al. (2005) from STSAT-1 and Datta et al. (1997) from sounding rocket  
 789 measurements. The energy spectra is soft for a typical microburst observed with  
 790 FIREBIRD-II and there was no statistically significant change in  $E_0$  for subsequent  
 791 bounces.

### 792 Microburst Scale Sizes

793 Lastly, after we applied the time and separation corrections detailed in Appendix  
 794 A, we mapped the locations of FU3 and FU4 in Fig. 2.3. The locations where FU3 saw  
 795 peaks 1-5 and where FU4 saw peaks 1-4 are shown as P1-5 and P1-4, respectively.

796 The lower bound on the latitudinal extent of the microburst was the difference in  
 797 latitude between P1 on FU3 and P4 on FU4 and was found to be  $29 \pm 1$  km. The  
 798 uncertainty was estimated from the spacecraft separation uncertainty described in  
 799 Appendix A. This scale size is the largest reported by FIREBIRD-II.

800 In section 2, we showed that the observed decaying peaks were likely due to  
 801 bouncing, so we assume that the observed electrons in subsequent bounces were the  
 802 drifted electrons from the initial microburst. Under this assumption, the scattered  
 803 electrons observed in the last bounce by FIREBIRD-II, must have drifted east from  
 804 their initial scattering longitude, allowing us to calculate the minimum longitudinal  
 805 scale size. Following geometrical arguments, the distance that electrons drift east in  
 806 a single bounce is a product of the circumference of the drift shell foot print, and the  
 807 fraction of the total drift orbit traversed in a single bounce and is given by,

$$d_{az} = 2\pi(R_E + A) \cos(\lambda) \frac{t_b}{\langle T_d \rangle} \quad (2.1)$$

where  $R_E$  is the Earth's radius,  $A$  is the spacecraft altitude,  $\lambda$  is the magnetic latitude,  
 $t_b$  is the electron bounce period, and  $\langle T_d \rangle$  is the electron drift period. Parks (2003)  
derived  $\langle T_d \rangle$  to be,

$$\langle T_d \rangle \approx \begin{cases} 43.8/(L \cdot E) & \text{if } \alpha_0 = 90^\circ \\ 62.7/(L \cdot E) & \text{if } \alpha_0 = 0^\circ \end{cases} \quad (2.2)$$

808 where  $E$  is the electron energy in MeV,  $L$  is the L shell, and  $\alpha_0$  is the equatorial pitch  
 809 angle. Electrons mirroring at FIREBIRD-II have  $\alpha_0 \approx 3.7^\circ$  and so the  $\alpha_0 = 0^\circ$  limit  
 810 was used.

811 The microburst's longitudinal scale size is defined as the distance the highest  
 812 energy electrons drifted in the time between the observations of the first and last  
 813 peaks. This scale size is given by  $D_{az} = n d_{az}$  where  $n$  is the number of bounces

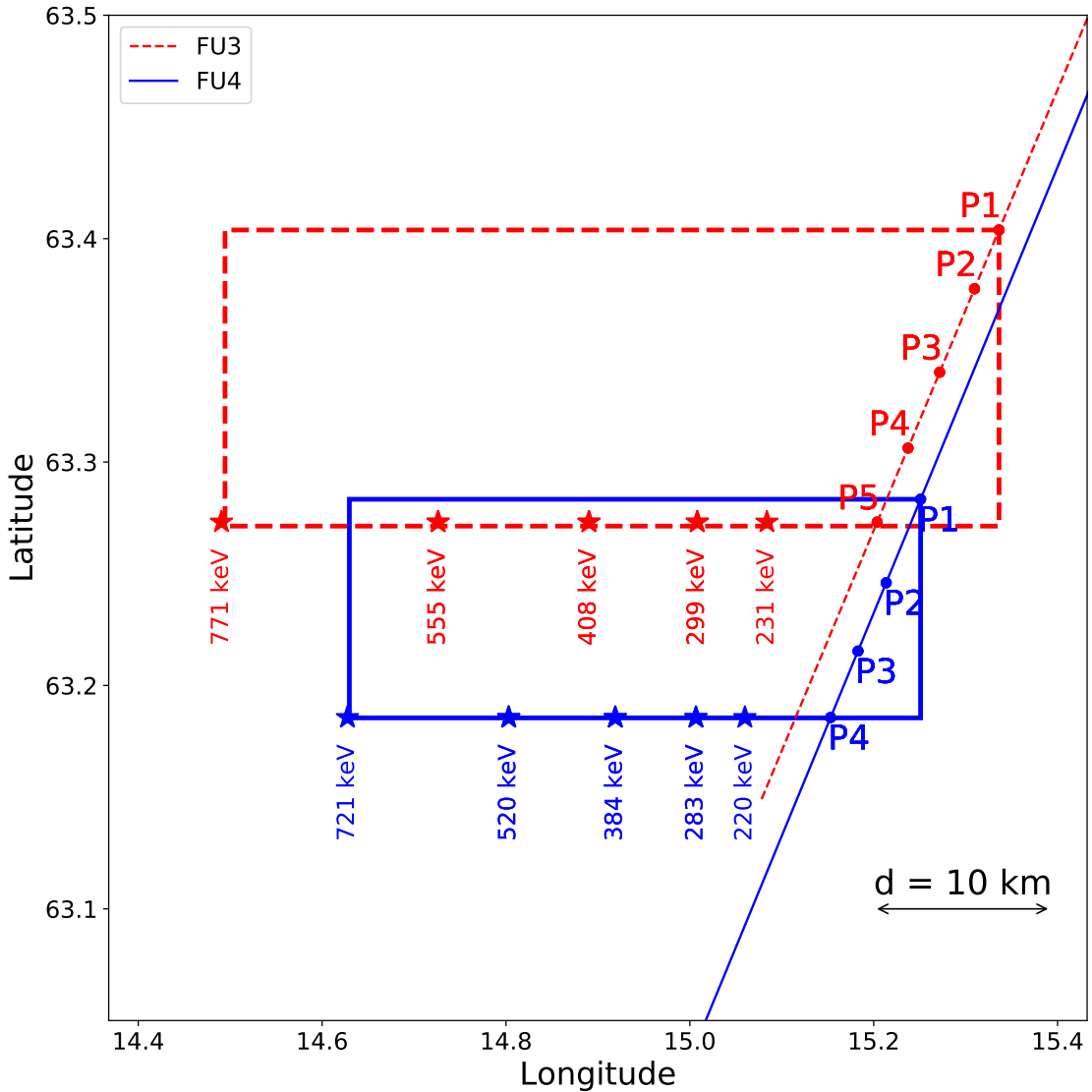


Figure 2.3: The topology of the FIREBIRD-II orbit and the multiple bounces of the microburst projected onto latitude and longitude with axis scaled to equal distance. Attributes relating to FU3 shown in red dashed lines, and FU4 with blue solid lines. The spacecraft path is shown with the diagonal lines, starting at the upper right corner. The labels P1-4 for FU4 and P1-5 for FU3 indicate where the spacecraft were when the  $N^{\text{th}}$  peak was seen in the lowest energy channel in the HiRes data. The stars with the accompanying energy labels represent the locations of the electrons with that energy that started at time of P1, and were seen at the last peak on each spacecraft. The rectangles represent the lower bound of the microburst scale size, assuming that the majority of the electrons were in the upper boundary of energy channel 4.

814 observed. The stars in Fig. 2.3 (with labels corresponding to energy channel  
 815 boundaries) represent the locations when the microburst was observed at P1, such  
 816 that an electron of that energy would drift eastward to be seen at P5 for FU3 and P4  
 817 for FU4. Since FU3 observed more peaks it observed the larger longitudinal scale size  
 818 which is shown with the red dashed box in Fig. 2.3. FU3's fourth energy channel's  
 819 bounds are 555 keV and 771 keV, which correspond to longitudinal distances of  $39 \pm 1$   
 820 km and  $51 \pm 1$ , respectively. The uncertainty was estimated by propagating the  
 821 uncertainty in the bounce time Eq. 2.1. While the observed minimum longitudinal  
 822 scale size is dependent on FIREBIRD-II's energy channels, the true scale size may  
 823 not be.

824 To investigate how the microburst scale size compares to the scale sizes of chorus  
 825 waves near the magnetic equator, the microburst's longitudinal and latitudinal scale  
 826 sizes and their uncertainties in LEO were mapped to the magnetic equator with T89.  
 827 The radial scale size (latitudinal scale mapped from LEO) was greater than  $500 \pm 10$   
 828 km. The azimuthal scale size (longitudinal scale mapped from LEO) of 555 keV  
 829 electrons was greater than  $450 \pm 10$  km and for the 771 keV electrons it was greater  
 830 than  $530 \pm 10$  km. The lower bound microburst scale size is similar to the chorus  
 831 scale sizes derived by Agapitov et al. (2017, 2011), and is discussed below.

832

### Discussion and Conclusions

833 We presented the first observation of a large microburst with multiple bounces  
 834 made possible by the twin FIREBIRD-II CubeSats. The microburst's lower bound  
 835 LEO latitudinal and longitudinal scale sizes of  $29 \pm 1$  km and  $51 \pm 1$  km make  
 836 it one of the largest observed. The microburst's LEO scale size was larger than  
 837 the latitudinal scale sizes of typical  $\gtrsim 1$  MeV microbursts reported in Blake et al.  
 838 (1996), approximately 10 times larger than reported in Dietrich et al. (2010), and

839 approximately 2.6 times larger than other simultaneous microbursts observed by  
 840 FIREBIRD-II (Crew et al., 2016). Lastly, the scale sizes derived here were similar to  
 841 the scale sizes of  $\gtrsim$  15 keV microbursts observed with a high altitude balloon (Parks,  
 842 1967). No energy dependence on the minimum latitudinal scale size was observed,  
 843 while the observed energy dependence of the minimum longitudinal scale size is an  
 844 artifact of the technique we used to estimate their drift motion.

845 The microburst scale size obtained in Section 2 and scaled to the geomagnetic  
 846 equator can be compared with the scales of chorus waves presumably responsible for  
 847 the rapid burst electron precipitation. Early direct estimates of the chorus source  
 848 scales were made by the coordinated measurement by ISEE-1, 2. The wave power  
 849 correlation scale was estimated to be about several hundred kilometers across the  
 850 background magnetic field (Gurnett et al., 1979). Furthermore, Santolik et al. (2003)  
 851 determined the correlation lengths of chorus-type whistler waves to be around 100  
 852 km based on multipoint CLUSTER Wide Band Data measurements near the chorus  
 853 source region at  $L \approx 4$ , during the magnetic storm of 18 April 2002. Agapitov et al.  
 854 (2017, 2011, 2010) recently showed that the spatial extent of chorus source region can  
 855 be larger, ranging from 600 km in the outer radiation belt to more than 1000 km in  
 856 the outer magnetosphere. The lower bound azimuthal and latitudinal scales obtained  
 857 in Section 2 and scaled to the magnetic equator, are similar to the whistler-mode  
 858 chorus source scale sizes reported in Agapitov et al. (2017, 2011).

859 No wave measurements from nearby spacecraft were available at this time.  
 860 Nevertheless, during the hours before and after this observation, the Van Allen Probes'  
 861 (Mauk et al., 2013) Electric and Magnetic Field Instrument and Integrated Science  
 862 (Kletzing et al., 2013) observed strong wave power in the lower band chorus frequency  
 863 range, inside the outer radiation belt between 22 and 2 MLT. Furthermore, AE  $\sim 400$   
 864 nT at this time, and relatively strong chorus waves were statistically more likely to

865 be present at FIREBIRD-II's MLT (Li et al., 2009).

866 The empirically estimated and modeled  $t_b$  in this study agree within FIREBIRD-  
 867 II's uncertainties, confirming that the energy-dependent dispersion was due to  
 868 bouncing. The  $t_b$  curves are a proxy for field line length, and this agreement implies  
 869 that they are comparable. This is expected since the magnetosphere is not drastically  
 870 compressed at 8 MLT, but we expect a larger discrepancy near midnight, where the  
 871 magnetosphere is more stretched and difficult to accurately model. In future studies,  
 872 this analysis can be used as a diagnostic tool to validate field line lengths, and improve  
 873 magnetic field models.

874 The similarity of the microburst and chorus source region scale sizes, as well  
 875 as magnetospheric location and conditions, further support the causal relationship  
 876 between microbursts and chorus.

877

### Acknowledgments

878 This work was made possible with help from the FIREBIRD team, and the  
 879 members of the Space Sciences and Engineering Laboratory at Montana State  
 880 University for their hard work to make this mission a success. In addition, M.  
 881 Shumko acknowledges Drew Turner for his suggestions regarding the bounce period  
 882 calculations, and Dana Longcope for his proofreading feedback. The FIREBIRD-II  
 883 data are available at [http://solar.physics.montana.edu/FIREBIRD\\_II/](http://solar.physics.montana.edu/FIREBIRD_II/). This analysis  
 884 is supported by the National Science Foundation under Grant Numbers 0838034 and  
 885 1339414. Furthermore, the work of O. Agapitov was supported by the NASA grant  
 886 NNX16AF85G.

## CONCLUSION

888        L<sup>A</sup>T<sub>E</sub>X produces documents that look great, automatically handles references and  
889 citations, and easily incorporates figures and tables. This is not a guide to L<sup>A</sup>T<sub>E</sub>X but  
890 rather an introduction to the MSU style. If you want more information about L<sup>A</sup>T<sub>E</sub>X  
891 many introductory guides can be found online.

## Bibliography

- 893 Abel, B. and Thorne, R. M. (1998). Electron scattering loss in earth's inner  
894 magnetosphere: 1. dominant physical processes. *Journal of Geophysical Research: Space Physics*, 103(A2):2385–2396.
- 896 Agapitov, O., Blum, L. W., Mozer, F. S., Bonnell, J. W., and Wygant, J. (2017).  
897 Chorus whistler wave source scales as determined from multipoint van allen probe  
898 measurements. *Geophysical Research Letters*, pages n/a–n/a. 2017GL072701.
- 899 Agapitov, O., Krasnoselskikh, V., Dudok de Wit, T., Khotyaintsev, Y., Pickett,  
900 J. S., Santolik, O., and Rolland, G. (2011). Multispacecraft observations of chorus  
901 emissions as a tool for the plasma density fluctuations' remote sensing. *Journal of Geophysical Research: Space Physics*, 116(A9):n/a–n/a. A09222.
- 903 Agapitov, O., Krasnoselskikh, V., Zaliznyak, Y., Angelopoulos, V., Le Contel, O.,  
904 and Rolland, G. (2010). Chorus source region localization in the earth's outer  
905 magnetosphere using themis measurements. *Annales Geophysicae*, 28(6):1377–  
906 1386.
- 907 Anderson, B., Shekhar, S., Millan, R., Crew, A., Spence, H., Klumpar, D., Blake, J.,  
908 O'Brien, T., and Turner, D. (2017). Spatial scale and duration of one microburst  
909 region on 13 August 2015. *Journal of Geophysical Research: Space Physics*.
- 910 Anderson, K. A. and Milton, D. W. (1964). Balloon observations of X rays in the  
911 auroral zone: 3. High time resolution studies. *Journal of Geophysical Research*,  
912 69(21):4457–4479.
- 913 Barcus, J., Brown, R., and Rosenberg, T. (1966). Spatial and temporal character of  
914 fast variations in auroral-zone x rays. *Journal of Geophysical Research*, 71(1):125–  
915 141.
- 916 Baumjohann, W. and Treumann, R. A. (1997). *Basic space plasma physics*. World  
917 Scientific.
- 918 Blake, J.,Looper, M., Baker, D., Nakamura, R., Klecker, B., and Hovestadt, D.  
919 (1996). New high temporal and spatial resolution measurements by sampex of the  
920 precipitation of relativistic electrons. *Advances in Space Research*, 18(8):171 – 186.
- 921 Blake, J. B. and O'Brien, T. P. (2016). Observations of small-scale latitudinal  
922 structure in energetic electron precipitation. *Journal of Geophysical Research: Space Physics*, 121(4):3031–3035. 2015JA021815.
- 924 Blum, L., Li, X., and Denton, M. (2015). Rapid MeV electron precipitation as  
925 observed by SAMPEX/HILT during high-speed stream-driven storms. *Journal of Geophysical Research: Space Physics*, 120(5):3783–3794. 2014JA020633.

- 927 Boscher, D., Bourdarie, S., O'Brien, P., Guild, T., and Shumko, M. (2012). Irbem-lib  
 928 library.
- 929 Breneman, A., Crew, A., Sample, J., Klumpar, D., Johnson, A., Agapitov, O.,  
 930 Shumko, M., Turner, D., Santolik, O., Wygant, J., et al. (2017). Observations  
 931 directly linking relativistic electron microbursts to whistler mode chorus: Van allen  
 932 probes and FIREBIRD II. *Geophysical Research Letters*.
- 933 Breneman, A. W., Halford, A., Millan, R., McCarthy, M., Fennell, J., Sample, J.,  
 934 Woodger, L., Hospodarsky, G., Wygant, J. R., Cattell, C. A., et al. (2015). Global-  
 935 scale coherence modulation of radiation-belt electron loss from plasmaspheric hiss.  
 936 *Nature*, 523(7559):193.
- 937 Brown, R., Barcus, J., and Parsons, N. (1965). Balloon observations of auroral zone  
 938 x rays in conjugate regions. 2. microbursts and pulsations. *Journal of Geophysical  
 939 Research (U.S.)*.
- 940 Capannolo, L., Li, W., Ma, Q., Shen, X.-C., Zhang, X.-J., Redmon, R., Rodriguez,  
 941 J., Engebretson, M., Kletzing, C., Kurth, W., et al. (2019). Energetic electron  
 942 precipitation: multi-event analysis of its spatial extent during emic wave activity.  
 943 *Journal of Geophysical Research: Space Physics*.
- 944 Claudepierre, S., O'Brien, T., Looper, M., Blake, J., Fennell, J., Roeder, J.,  
 945 Clemmons, J., Mazur, J., Turner, D., Reeves, G., et al. (2019). A revised look  
 946 at relativistic electrons in the earth's inner radiation zone and slot region. *Journal  
 947 of Geophysical Research: Space Physics*, 124(2):934–951.
- 948 Comess, M., Smith, D., Selesnick, R., Millan, R., and Sample, J. (2013). Duskside  
 949 relativistic electron precipitation as measured by sampex: A statistical survey.  
 950 *Journal of Geophysical Research: Space Physics*, 118(8):5050–5058.
- 951 Crew, A. B., Spence, H. E., Blake, J. B., Klumpar, D. M., Larsen, B. A., O'Brien,  
 952 T. P., Driscoll, S., Handley, M., Legere, J., Longworth, S., Mashburn, K.,  
 953 Mosleh, E., Ryhajlo, N., Smith, S., Springer, L., and Widholm, M. (2016). First  
 954 multipoint in situ observations of electron microbursts: Initial results from the  
 955 NSF FIREBIRD II mission. *Journal of Geophysical Research: Space Physics*,  
 956 121(6):5272–5283. 2016JA022485.
- 957 Datta, S., Skoug, R., McCarthy, M., and Parks, G. (1997). Modeling of microburst  
 958 electron precipitation using pitch angle diffusion theory. *Journal of Geophysical  
 959 Research: Space Physics*, 102(A8):17325–17333.
- 960 Dietrich, S., Rodger, C. J., Clilverd, M. A., Bortnik, J., and Raita, T. (2010).  
 961 Relativistic microburst storm characteristics: Combined satellite and ground-based  
 962 observations. *Journal of Geophysical Research: Space Physics*, 115(A12).

- 963 Douma, E., Rodger, C. J., Blum, L. W., and Clilverd, M. A. (2017). Occurrence  
 964 characteristics of relativistic electron microbursts from SAMPEX observations.  
 965 *Journal of Geophysical Research: Space Physics*, 122(8):8096–8107. 2017JA024067.
- 966 Dungey, J. W. (1961). Interplanetary magnetic field and the auroral zones. *Phys.  
 967 Rev. Lett.*, 6:47–48.
- 968 Fang, X., Randall, C. E., Lummerzheim, D., Wang, W., Lu, G., Solomon, S. C., and  
 969 Frahm, R. A. (2010). Parameterization of monoenergetic electron impact ionization.  
 970 *Geophysical Research Letters*, 37(22).
- 971 Greeley, A., Kanekal, S., Baker, D., Klecker, B., and Schiller, Q. (2019). Quantifying  
 972 the contribution of microbursts to global electron loss in the radiation belts. *Journal  
 973 of Geophysical Research: Space Physics*.
- 974 Gurnett, D., Anderson, R., Scarf, F., Fredricks, R., and Smith, E. (1979). Initial  
 975 results from the isee-1 and-2 plasma wave investigation. *Space Science Reviews*,  
 976 23(1):103–122.
- 977 Hendry, A. T., Rodger, C. J., and Clilverd, M. A. (2017). Evidence of sub-mev  
 978 emic-driven electron precipitation. *Geophysical Research Letters*, 44(3):1210–1218.
- 979 Hoots, F. R. and Roehrich, R. L. (1980). Models for propagation of norad element  
 980 sets. Technical Report 3, Spacetrack.
- 981 Horne, R., Glauert, S., Meredith, N., Boscher, D., Maget, V., Heynderickx, D., and  
 982 Pitchford, D. (2013). Space weather impacts on satellites and forecasting the earth's  
 983 electron radiation belts with spacecast. *Space Weather*, 11(4):169–186.
- 984 Horne, R. B. and Thorne, R. M. (2003). Relativistic electron acceleration and  
 985 precipitation during resonant interactions with whistler-mode chorus. *Geophysical  
 986 Research Letters*, 30(10). 1527.
- 987 Horne, R. B., Thorne, R. M., Shprits, Y. Y., Meredith, N. P., Glauert, S. A., Smith,  
 988 A. J., Kanekal, S. G., Baker, D. N., Engebretson, M. J., Posch, J. L., et al.  
 989 (2005). Wave acceleration of electrons in the van allen radiation belts. *Nature*,  
 990 437(7056):227.
- 991 Kasahara, S., Miyoshi, Y., Yokota, S., Mitani, T., Kasahara, Y., Matsuda, S.,  
 992 Kumamoto, A., Matsuoka, A., Kazama, Y., Frey, H., et al. (2018). Pulsating  
 993 aurora from electron scattering by chorus waves. *Nature*, 554(7692):337.
- 994 Kletzing, C., Kurth, W., Acuna, M., MacDowall, R., Torbert, R., Averkamp, T.,  
 995 Bodet, D., Bounds, S., Chutter, M., Connerney, J., et al. (2013). The electric and  
 996 magnetic field instrument suite and integrated science (EMFISIS) on RBSP. *Space  
 997 Science Reviews*, 179(1-4):127–181.

- 998 Klumpar, D., Springer, L., Mosleh, E., Mashburn, K., Berardinelli, S., Gunderson,  
 999 A., Handly, M., Ryhajlo, N., Spence, H., Smith, S., Legere, J., Widholm, M.,  
 1000 Longworth, S., Crew, A., Larsen, B., Blake, J., and Walmsley, N. (2015). Flight  
 1001 system technologies enabling the twin-cubesat firebird-ii scientific mission.
- 1002 Lee, J. J., Parks, G. K., Lee, E., Tsurutani, B. T., Hwang, J., Cho, K. S., Kim, K.-H.,  
 1003 Park, Y. D., Min, K. W., and McCarthy, M. P. (2012). Anisotropic pitch angle  
 1004 distribution of 100 keV microburst electrons in the loss cone: measurements from  
 1005 STSAT-1. *Annales Geophysicae*, 30(11):1567–1573.
- 1006 Lee, J.-J., Parks, G. K., Min, K. W., Kim, H. J., Park, J., Hwang, J., McCarthy,  
 1007 M. P., Lee, E., Ryu, K. S., Lim, J. T., Sim, E. S., Lee, H. W., Kang, K. I., and  
 1008 Park, H. Y. (2005). Energy spectra of 170–360 keV electron microbursts measured  
 1009 by the korean STSAT-1. *Geophysical Research Letters*, 32(13). L13106.
- 1010 Li, W., Thorne, R. M., Angelopoulos, V., Bortnik, J., Cully, C. M., Ni, B., LeContel,  
 1011 O., Roux, A., Auster, U., and Magnes, W. (2009). Global distribution of whistler-  
 1012 mode chorus waves observed on the THEMIS spacecraft. *Geophysical Research  
 1013 Letters*, 36(9). L09104.
- 1014 Li, X., Selesnick, R., Schiller, Q., Zhang, K., Zhao, H., Baker, D. N., and Temerin,  
 1015 M. A. (2017). Measurement of electrons from albedo neutron decay and neutron  
 1016 density in near-earth space. *Nature*, 552(7685):382.
- 1017 Lorentzen, K. R., Blake, J. B., Inan, U. S., and Bortnik, J. (2001a). Observations  
 1018 of relativistic electron microbursts in association with VLF chorus. *Journal of  
 1019 Geophysical Research: Space Physics*, 106(A4):6017–6027.
- 1020 Lorentzen, K. R., Looper, M. D., and Blake, J. B. (2001b). Relativistic electron  
 1021 microbursts during the GEM storms. *Geophysical Research Letters*, 28(13):2573–  
 1022 2576.
- 1023 Lyons, L. R. and Thorne, R. M. (1973). Equilibrium structure of radiation belt  
 1024 electrons. *Journal of Geophysical Research*, 78(13):2142–2149.
- 1025 Mauk, B., Fox, N. J., Kanekal, S., Kessel, R., Sibeck, D., and Ukhorskiy, A. (2013).  
 1026 Science objectives and rationale for the radiation belt storm probes mission. *Space  
 1027 Science Reviews*, 179(1-4):3–27.
- 1028 Meredith, N., Horne, R., Summers, D., Thorne, R., Iles, R., Heynderickx, D., and  
 1029 Anderson, R. (2002). Evidence for acceleration of outer zone electrons to relativistic  
 1030 energies by whistler mode chorus. In *Annales Geophysicae*, volume 20, pages 967–  
 1031 979.
- 1032 Millan, R. and Thorne, R. (2007). Review of radiation belt relativistic electron losses.  
 1033 *Journal of Atmospheric and Solar-Terrestrial Physics*, 69(3):362 – 377.

- 1034 Millan, R. M., Lin, R., Smith, D., Lorentzen, K., and McCarthy, M. (2002). X-  
 1035 ray observations of mev electron precipitation with a balloon-borne germanium  
 1036 spectrometer. *Geophysical research letters*, 29(24).
- 1037 Mozer, F. S., Agapitov, O. V., Blake, J. B., and Vasko, I. Y. (2018). Simultaneous  
 1038 observations of lower band chorus emissions at the equator and microburst  
 1039 precipitating electrons in the ionosphere. *Geophysical Research Letters*.
- 1040 Nakamura, R., Baker, D. N., Blake, J. B., Kanekal, S., Klecker, B., and Hovestadt,  
 1041 D. (1995). Relativistic electron precipitation enhancements near the outer edge of  
 1042 the radiation belt. *Geophysical Research Letters*, 22(9):1129–1132.
- 1043 Nakamura, R., Isowa, M., Kamide, Y., Baker, D., Blake, J., and Looper, M. (2000).  
 1044 Observations of relativistic electron microbursts in association with VLF chorus.  
 1045 *J. Geophys. Res.*, 105:15875–15885.
- 1046 O'Brien, T., Claudepierre, S., Blake, J., Fennell, J. F., Clemmons, J., Roeder, J.,  
 1047 Spence, H. E., Reeves, G., and Baker, D. (2014). An empirically observed pitch-  
 1048 angle diffusion eigenmode in the earth's electron belt near  $l^*= 5.0$ . *Geophysical*  
 1049 *Research Letters*, 41(2):251–258.
- 1050 O'Brien, T., Claudepierre, S., Guild, T., Fennell, J., Turner, D., Blake, J., Clemmons,  
 1051 J., and Roeder, J. (2016). Inner zone and slot electron radial diffusion revisited.  
 1052 *Geophysical Research Letters*, 43(14):7301–7310.
- 1053 O'Brien, T. and Moldwin, M. (2003). Empirical plasmapause models from magnetic  
 1054 indices. *Geophysical Research Letters*, 30(4).
- 1055 O'Brien, T. P., Looper, M. D., and Blake, J. B. (2004). Quantification of relativistic  
 1056 electron microburst losses during the GEM storms. *Geophysical Research Letters*,  
 1057 31(4). L04802.
- 1058 O'Brien, T. P., Lorentzen, K. R., Mann, I. R., Meredith, N. P., Blake, J. B., Fennell,  
 1059 J. F., Looper, M. D., Milling, D. K., and Anderson, R. R. (2003). Energization of  
 1060 relativistic electrons in the presence of ULF power and MeV microbursts: Evidence  
 1061 for dual ULF and VLF acceleration. *Journal of Geophysical Research: Space*  
 1062 *Physics*, 108(A8).
- 1063 Olson, W. P. and Pfitzer, K. A. (1982). A dynamic model of the magnetospheric  
 1064 magnetic and electric fields for july 29, 1977. *Journal of Geophysical Research:*  
 1065 *Space Physics*, 87(A8):5943–5948.
- 1066 Ozaki, M., Miyoshi, Y., Shiokawa, K., Hosokawa, K., Oyama, S.-i., Kataoka, R.,  
 1067 Ebihara, Y., Ogawa, Y., Kasahara, Y., Yagitani, S., et al. (2019). Visualization of  
 1068 rapid electron precipitation via chorus element wave-particle interactions. *Nature*  
 1069 *communications*, 10(1):257.

- 1070 Parks, G. (2003). *Physics Of Space Plasmas: An Introduction, Second Edition.*  
 1071 Westview Press.
- 1072 Parks, G. K. (1967). Spatial characteristics of auroral-zone X-ray microbursts. *Journal  
 1073 of Geophysical Research*, 72(1):215–226.
- 1074 Reeves, G., Spence, H. E., Henderson, M., Morley, S., Friedel, R., Funsten, H., Baker,  
 1075 D., Kanekal, S., Blake, J., Fennell, J., et al. (2013). Electron acceleration in the  
 1076 heart of the van allen radiation belts. *Science*, 341(6149):991–994.
- 1077 Reeves, G. D., McAdams, K. L., Friedel, R. H. W., and O'Brien, T. P. (2003). Ac-  
 1078 celeration and loss of relativistic electrons during geomagnetic storms. *Geophysical  
 1079 Research Letters*, 30(10):n/a–n/a. 1529.
- 1080 Santolik, O., Gurnett, D., Pickett, J., Parrot, M., and Cornilleau-Wehrlin, N. (2003).  
 1081 Spatio-temporal structure of storm-time chorus. *Journal of Geophysical Research:  
 1082 Space Physics*, 108(A7).
- 1083 Schulz, M. and Lanzerotti, L. J. (1974). *Particle Diffusion in the Radiation Belts.*  
 1084 Springer.
- 1085 Selesnick, R. S., Blake, J. B., and Mewaldt, R. A. (2003). Atmospheric losses of  
 1086 radiation belt electrons. *Journal of Geophysical Research: Space Physics*, 108(A12).  
 1087 1468.
- 1088 Shprits, Y. Y., Meredith, N. P., and Thorne, R. M. (2007). Parameterization  
 1089 of radiation belt electron loss timescales due to interactions with chorus waves.  
 1090 *Geophysical Research Letters*, 34(11):n/a–n/a. L11110.
- 1091 Shprits, Y. Y. and Thorne, R. M. (2004). Time dependent radial diffusion modeling  
 1092 of relativistic electrons with realistic loss rates. *Geophysical Research Letters*,  
 1093 31(8):n/a–n/a. L08805.
- 1094 Spence, H. E., Blake, J. B., Crew, A. B., Driscoll, S., Klumpar, D. M., Larsen,  
 1095 B. A., Legere, J., Longworth, S., Mosleh, E., O'Brien, T. P., Smith, S., Springer,  
 1096 L., and Widholm, M. (2012). Focusing on size and energy dependence of electron  
 1097 microbursts from the van allen radiation belts. *Space Weather*, 10(11).
- 1098 Summers, D., Thorne, R. M., and Xiao, F. (1998). Relativistic theory of wave-particle  
 1099 resonant diffusion with application to electron acceleration in the magnetosphere.  
 1100 *Journal of Geophysical Research: Space Physics*, 103(A9):20487–20500.
- 1101 Thorne, R. M. (2010). Radiation belt dynamics: The importance of wave-particle  
 1102 interactions. *Geophysical Research Letters*, 37(22). L22107.

- 1103 Thorne, R. M., O'Brien, T. P., Shprits, Y. Y., Summers, D., and Horne, R. B. (2005).  
 1104 Timescale for MeV electron microburst loss during geomagnetic storms. *Journal*  
 1105 *of Geophysical Research: Space Physics*, 110(A9). A09202.
- 1106 Trefall, H., Bjordal, J., Ullaland, S., and Stadsnes, J. (1966). On the extension of  
 1107 auroral-zone x-ray microbursts. *Journal of Atmospheric and Terrestrial Physics*,  
 1108 28(2):225–233.
- 1109 Tsurutani, B. T. and Lakhina, G. S. (1997). Some basic concepts of wave-particle  
 1110 interactions in collisionless plasmas. *Reviews of Geophysics*, 35(4):491–501.
- 1111 Tsyganenko, N. (1989). A solution of the chapman-ferraro problem for an ellipsoidal  
 1112 magnetopause. *Planetary and Space Science*, 37(9):1037 – 1046.
- 1113 Tsyganenko, N. A. and Sitnov, M. I. (2005). Modeling the dynamics of the inner  
 1114 magnetosphere during strong geomagnetic storms. *Journal of Geophysical Research:*  
 1115 *Space Physics*, 110(A3).
- 1116 Turner, D., Claudepierre, S., Fennell, J., O'Brien, T., Blake, J., Lemon, C.,  
 1117 Gkioulidou, M., Takahashi, K., Reeves, G., Thaller, S., et al. (2015). Energetic  
 1118 electron injections deep into the inner magnetosphere associated with substorm  
 1119 activity. *Geophysical Research Letters*, 42(7):2079–2087.
- 1120 Ukhorskiy, A. Y., Anderson, B. J., Brandt, P. C., and Tsyganenko, N. A. (2006).  
 1121 Storm time evolution of the outer radiation belt: Transport and losses. *Journal of*  
 1122 *Geophysical Research: Space Physics*, 111(A11):n/a–n/a. A11S03.
- 1123 Van Allen, J. A. (1959). The geomagnetically trapped corpuscular radiation. *Journal*  
 1124 *of Geophysical Research*, 64(11):1683–1689.
- 1125 Vernov, S. and Chudakov, A. (1960). Investigation of radiation in outer space. In  
 1126 *International Cosmic Ray Conference*, volume 3, page 19.
- 1127 Woodger, L., Halford, A., Millan, R., McCarthy, M., Smith, D., Bowers, G., Sample,  
 1128 J., Anderson, B., and Liang, X. (2015). A summary of the BARREL campaigns:  
 1129 Technique for studying electron precipitation. *Journal of Geophysical Research:*  
 1130 *Space Physics*, 120(6):4922–4935.

1131

## APPENDIX: APPENDIX A

1132 This appendix describes the method we used to calculate the time difference and  
 1133 separation between FU3 and FU4 at 06:12 UT on February 2nd, 2015.

1134

Time and position correction

1135 We used the following method to calculate the clock difference,  $\delta t_c$  and  
 1136 separation,  $d$  between FU3 and FU4 at 06:12 UT on February 2nd, 2015.

1137 The relative clock difference was calculated with a cross-correlation time  
 1138 lag analysis on uniquely-identified trains of microbursts that hit both spacecraft  
 1139 simultaneously. Four time periods with coincident microbursts were hand-picked on  
 1140 February 2nd, 2015 and are shown in Figs. A.1-A.4, panels (a) and (b). The cross-  
 1141 correlation time lag analysis was applied to the HiRes time series in panels (a) and  
 1142 (b), and the resulting normalized cross-correlation coefficient as a function of time is  
 1143 shown in panel (c). To validate the peak lag identified in panel (c), FU3's time series  
 1144 was shifted by that lag and is shown in panel (d).

1145 The clock differences from the simultaneous microbursts in Figs. A.1-A.4 were  
 1146 linearly fit to account for the relative clock drift ( $\approx 20$  ms/hour at this time), giving  
 1147 a value of  $\delta t_c = 2.28 \pm 0.12$  s at the time of the microburst analyzed here. This time  
 1148 shift was applied to the HiRes data in Fig. 1. A clock difference of  $\delta t_c = 2.45^{+0.51}_{-0.98}$  s  
 1149 was independently calculated with the FIREBIRD-II telemetry beacon time stamps  
 1150 that were downlinked during operational passes.

1151 We calculate the spacecraft separation, by applying same the cross-correlation  
 1152 time lag analysis on structures assumed to be spatial and are shown in Figs. A.5  
 1153 and A.6. The lag from the peak cross-correlation between these events is a sum of  
 1154 the clock difference and time lag due to the spacecraft separation. We interpret the  
 1155 time lag due to the spacecraft separation as the time difference between when the  
 1156 leading satellite observed a stationary spatial feature, to when the trailing satellite  
 1157 observed the same stationary spatial feature. With the method described above, we  
 1158 find the spatial time lag to be  $\delta t_d = 2.64 \pm 0.12$  s (after we account for the clock  
 1159 difference and its uncertainty). To convert from a spatial time lag to a spacecraft  
 1160 separation, we calculate the satellite velocity. We calculate the velocity using a Two  
 1161 Line Element (TLE), a data format containing the orbit parameters that are used  
 1162 for orbit propagation. With the TLE derived spacecraft velocity,  $v = 7.57$  km/s, the  
 1163 spacecraft separation was  $d = 19.9 \pm 0.9$  km.

1164 An independent method to calculate the spacecraft separation was developed.  
 1165 The separation was calculated using TLEs. The TLE from February 2nd was  
 1166 anomalous and was not used in this analysis. Instead, seven TLEs released up to  
 1167 five days after the microburst event were backpropagated, using the SGP-4 algorithm

1168 (Hoots and Roehrich, 1980) that calculates orbital state vectors with perturbations  
1169 such as Earth's atmosphere, as well as gravitational effects from the moon and sun.  
1170 Then the predicted spacecraft separations at the time of the microburst event were  
1171 averaged to derive a separation of  $d = 18.4 \pm 1.5$  km. These two methods give  
1172 similar separations, which implies that the stationary event assumption used in the  
1173 cross-correlation time lag analysis is reasonable.

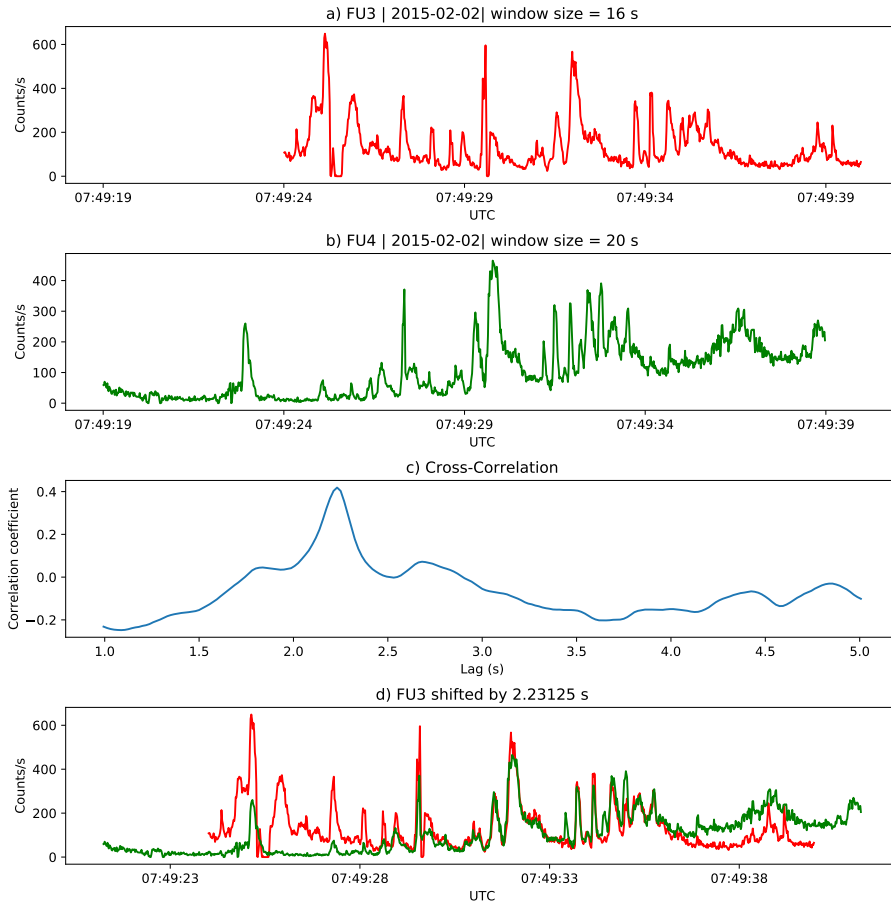


Figure A.1: Cross-correlation time lag analysis applied to a train of microbursts. Panel (a) and (b) show the count rate from the lowest energy channel. Panel (c) shows the cross-correlation coefficient as a function of time lag. Panel (d) shows the shifted timeseries. Clock difference was 2.23 s.

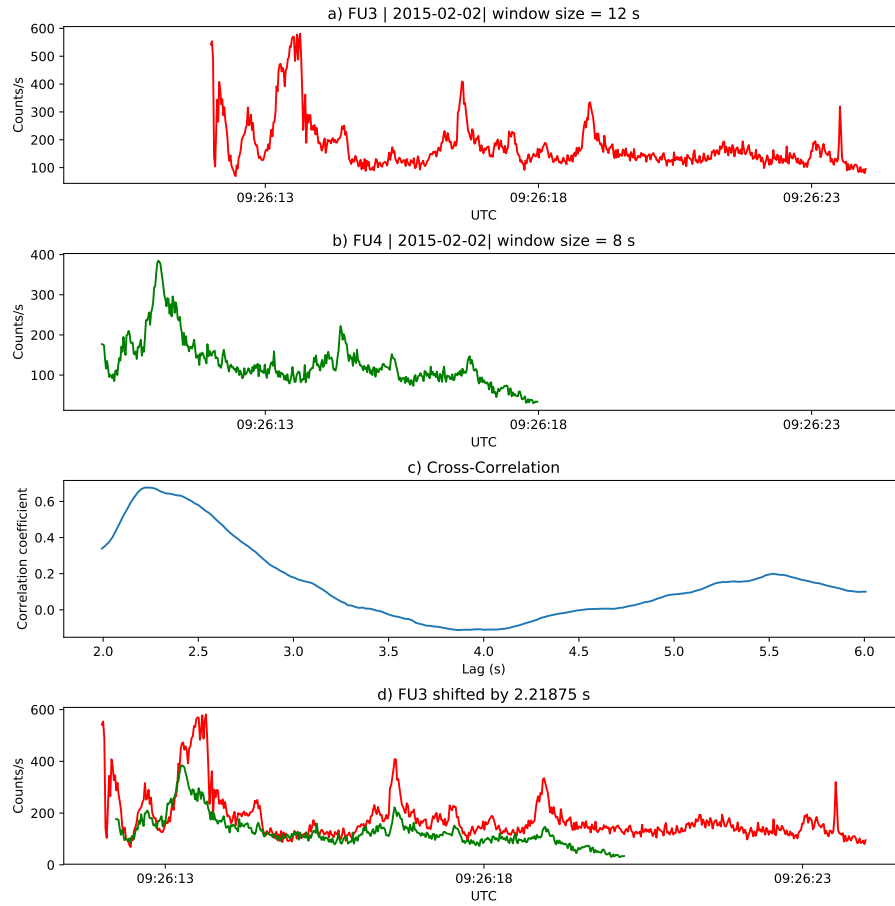


Figure A.2: Same analysis as Fig. A.1 on a different time period. Clock difference was 2.21 s.

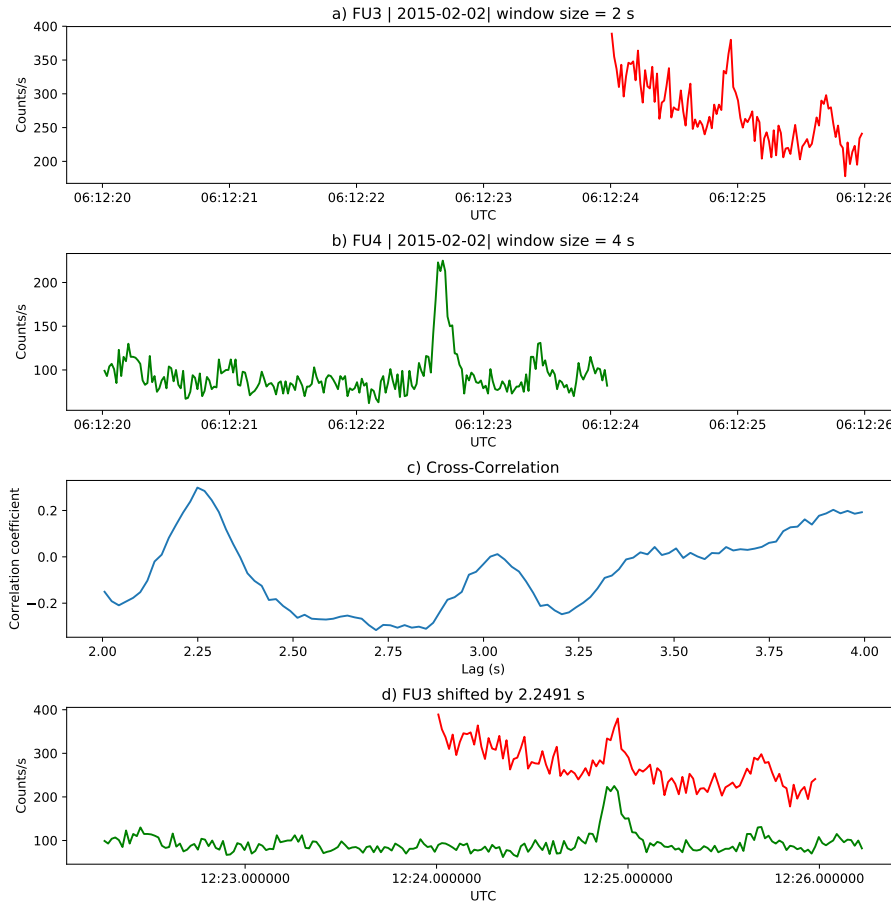


Figure A.3: Same analysis as Fig. A.1 on a different time period. Clock difference was 2.25 s.

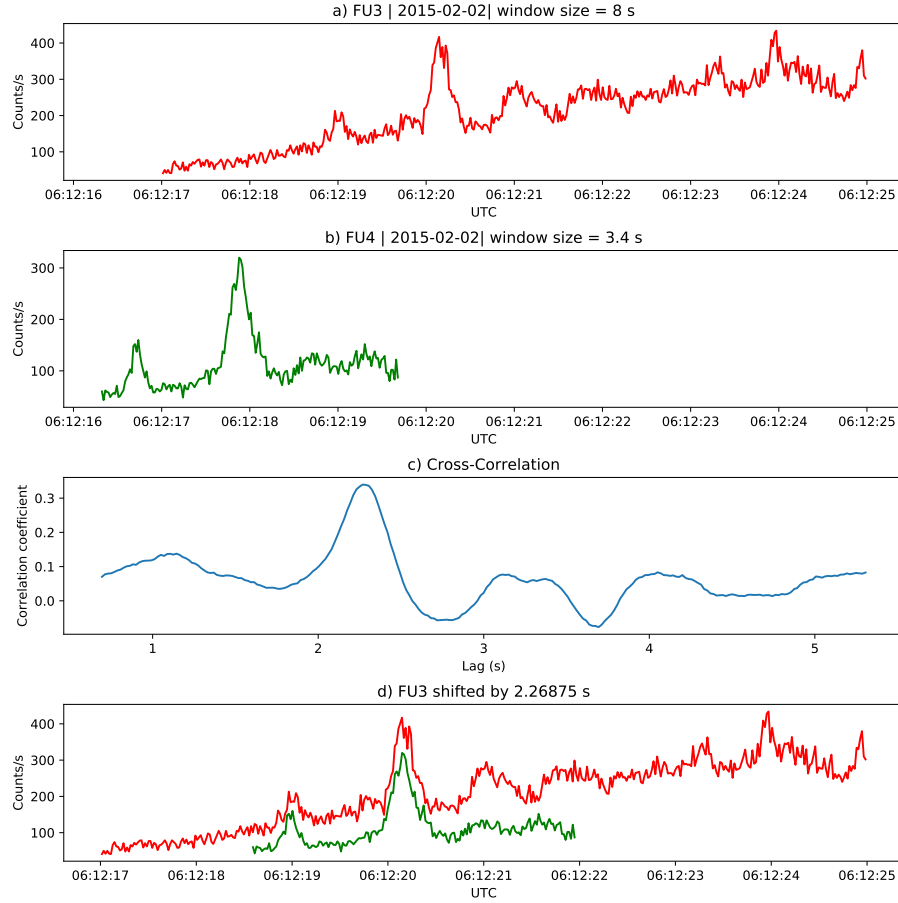


Figure A.4: Same analysis as Fig. A.1 on a different time period. Clock difference was 2.27 s.

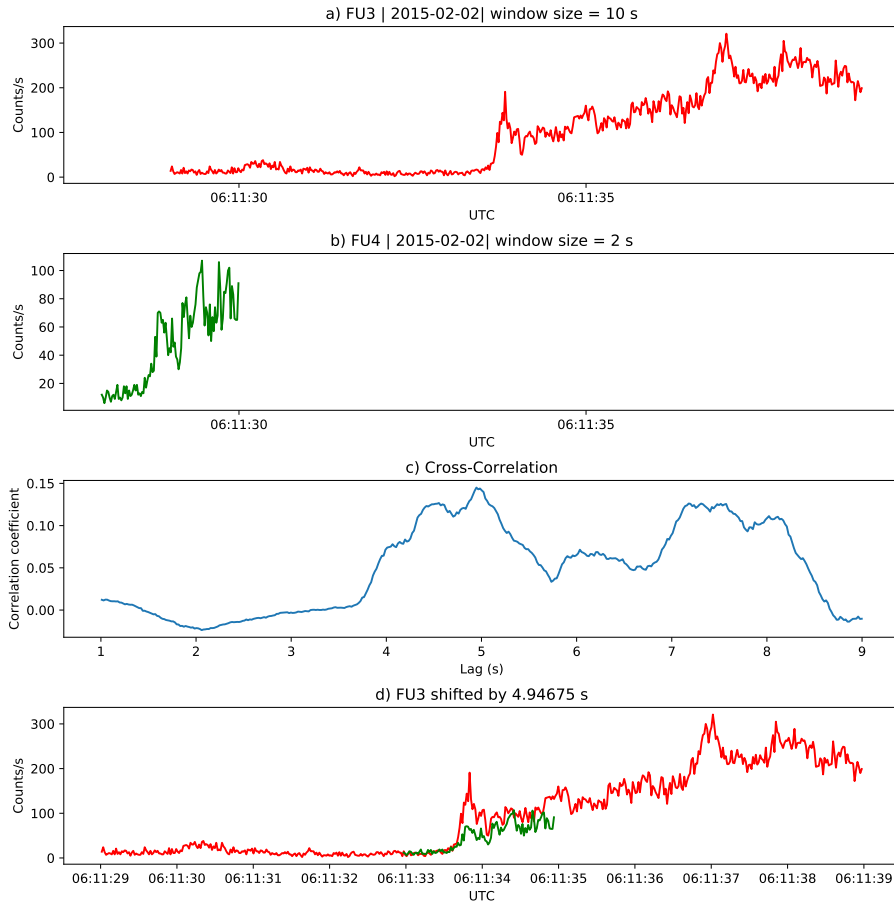


Figure A.5: Same cross-correlation time lag analysis applied to stationary spatial structures. The cross-correlation lag between these events is a sum of the clock difference and time lag due to the spacecraft separation. The lag derived at this time was 4.95 s.

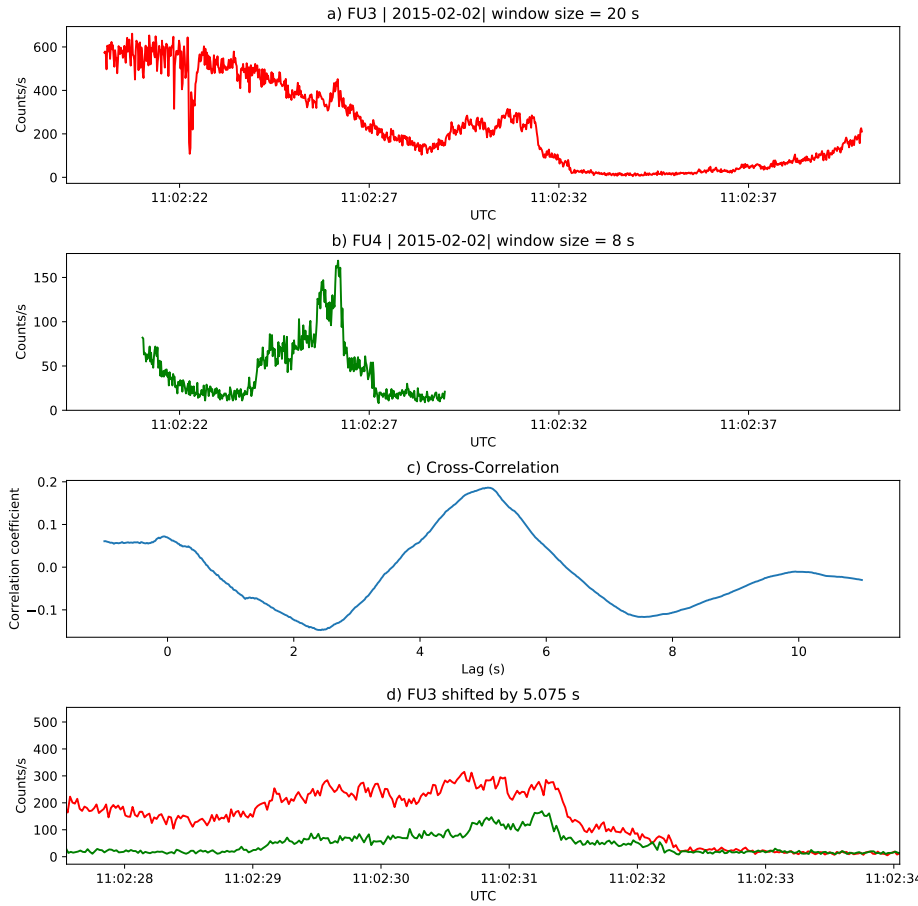


Figure A.6: Same analysis as Fig. A.5 applied to a different stationary spatial feature. The lag derived at this time was 5.01 s.